AWARD NUMBER: W81XWH-14-1-0192

TITLE: Next-Generation Molecular Histology Using Highly Multiplexed Ion-Beam Imaging (MIBI) of Breast Cancer Tissue Specimens for Enhanced Clinical Guidance

PRINCIPAL INVESTIGATOR: **Alexander Borowsky**

CONTRACTING ORGANIZATION: **University of California, Davis**
Davis, CA 95618

REPORT DATE: **January 2018**

TYPE OF REPORT: **Final**

PREPARED FOR: U.S. Army Medical Research and Materiel Command
Fort Detrick, Maryland 21702-5012

DISTRIBUTION STATEMENT: Approved for public release, distribution unlimited.

REPORT DOCUMENTATION PAGE

Form Approved
OMB No. 0704-0188

1. REPORT DATE
January 2018

2. REPORT TYPE
Final Report

3. DATES COVERED
7/1/14-10/31/17

4. TITLE AND SUBTITLE
Next-Generation Molecular Histology Using Highly Multiplexed Ion-Beam Imaging (MIBI) of Breast Cancer Tissue Specimens for Enhanced Clinical Guidance

5a. CONTRACT NUMBER

5b. GRANT NUMBER
W81XWH-14-1-0192

5c. PROGRAM ELEMENT NUMBER

6. AUTHOR(S)
Alexander Borowsky

E-Mail:adborowsky@ucdavis.edu

5d. PROJECT NUMBER

5e. TASK NUMBER

5f. WORK UNIT NUMBER

7. PERFORMING ORGANIZATION NAME(S) AND ADDRESS(ES)

University of California
Davis, One Shields Ave
Davis, CA 95616

8. PERFORMING ORGANIZATION REPORT NUMBER

9. SPONSORING / MONITORING AGENCY NAME(S) AND ADDRESS(ES)

U.S. Army Medical Research and Materiel Command
Fort Detrick, Maryland 21702-5012

10. SPONSOR/MONITOR'S ACRONYM(S)

11. SPONSOR/MONITOR'S REPORT NUMBER(S)

12. DISTRIBUTION / AVAILABILITY STATEMENT

Approved for Public Release; Distribution Unlimited

13. SUPPLEMENTARY NOTES

14. ABSTRACT

The ability to visualize the presence, abundance, location and functional state of many proteins at once in cells and tissues with preserved morphology has long been a goal. This proposal seeks to optimize recently demonstrated mass-spec-based imaging methods that can, when fully developed, detect as many as 40 to 100+ molecular targets in cells and tissues using simultaneously applied mass-tag-labeled antibodies, with outstanding morphology. Preliminary data using a highly focused, scanning oxygen ion beam and 10 antibodies applied simultaneously to clinical breast cancer tissues demonstrate histology-like images that reveal bound antibody location with subcellular resolution. The present project will address: reliable pre analytical sample preparation methods and labeling techniques for protein analytes; ion-beam imaging method improvements based on current and projected instrumentation; powerful, easy-to-use software for equipment control, display and analysis; and validation in several important biological test cases. Going forward, we would like to optimize sensitivity and reliability, with the goal of making this a standard, high performance, imaging approach for basic and translational science discovery, drug development, and possible clinical deployment.

15. SUBJECT TERMS
Breast Cancer Diagnosis, Pathology, Immunophenotype, Multiplex, Morphology, RNA In Situ Hybridization, Immunohistochemistry/Immunofluorescence, Predictive Biomarkers

16. SECURITY CLASSIFICATION OF:			17. LIMITATION OF ABSTRACT	18. NUMBER OF PAGES	19a. NAME OF RESPONSIBLE PERSON USAMRMC
a. REPORT Unclassified	b. ABSTRACT Unclassified	c. THIS PAGE Unclassified	Unclassified	39	19b. TELEPHONE NUMBER *(include area code)*

TABLE OF CONTENTS

Page

8. **Special Reporting Requirements**
9. **Appendices**

1. INTRODUCTION

The ability to visualize the presence, abundance, location and functional state of many proteins at once in cells and tissues with preserved morphology has long been a goal. This proposal seeks to optimize recently demonstrated mass-spec-based imaging methods that can, when fully developed, detect as many as 40 to100+ molecular targets in cells and tissues using simultaneously applied mass-tag-labeled antibodies, with outstanding morphology. The technique is analogous to laser-scanning confocal microscopy, except that the scanning is performed using a tightly focused ion beam, rather than a similarly sized point of laser light. And instead of fluorophores, the labels detected are clusters of metal atoms attached to any given probe. When ionized and collected at a detector, these metal species can be unambiguously distinguished based on their mass (atomic weight). Preliminary data using a highly focused, scanning oxygen ion beam and 10 antibodies applied simultaneously to clinical breast cancer tissues demonstrate histology-like images that reveal bound antibody location with subcellular resolution. Going forward, we would like to optimize sensitivity and reliability, with the goal of making this a standard, high-performance, imaging approach for basic and translational science discovery, drug development, and possible clinical deployment. The present project will address: reliable pre-analytical sample preparation methods and labeling techniques for protein analytes; ion-beam imaging method improvements based on current and projected instrumentation; powerful, easy-to-use software for equipment control, display and analysis; and validation in several important biological test cases.

2. KEYWORDS

Imaging, mass spec, tissue morphology, multiplex ion beam imaging, metal isotopes, breast cancer, pre-analytical sample preparation.

3. ACCOMPLISHMENTS

SOW (joint UC Davis and Stanford).

MIBI (multiplex ion beam imaging) using mass-tagged probes, developed in collaboration between UC Davis Pathology and Stanford University, dramatically improves upon standard histology, immunohistochemistry (IHC), and in situ hybridization (ISH) methods, with up to 100-fold multiplexing at subcellular resolution (in review, Nature Methods). We propose to apply this approach to breast cancer profiling. Current breast cancer diagnosis includes predictive assays to guide therapy decisions, involving a minimum of 3 assays: ER, PR, and HER2. Many labs also include a marker of proliferation (Ki67), and sometimes myoepithelial (SMA), epithelial (CK8/18), and lobular markers (ECAD). Recently, a host of new multi-marker panels developed. The "Mammostrat" assay (Clarient) uses a panel of five IHC markers (P53, SLC7A5, NRDG1, HTF9C, CEACAM5). Gene-expression assays using qRT-PCR, array hybridization, and RNA sequence assays have also been developed. The OncotypeDX, for example, uses a panel of 21 genes (16 analytical, 5 controls: Ki67, STK15, Survivin, CCNB1, MYBL2, MMP11, CTSL2, HER2, GRB7, GSTM1, CD68, BAG1, ER, PGR, BCL2, SCUBE2, ACTB, GAPDH, RPLPO, GUS, TFRC) to stratify risk of recurrence, and relative benefit of adjuvant chemotherapy. This explosion in biomarkers poses both cost and logical selection challenges. In addition, these assays generally lose all spatial context information (including heterogeneity). MIBI technology provides the potential to simultaneously assay all of the relevant analytes in an intact tissue architecture, with submicron resolution and a greatly expanded dynamic range of quantitation. We propose to develop assays and analysis tools to evaluate breast cancer tissues using formal fixed and paraffin embedded tumor tissues from the clinic, and we will compare the utility of the MIBI platform assays to the current assays. We believe that we can replace and improve upon the current assays, at a fraction of the cost.

The Stanford work involves imaging on the MIBI SIMS instrument, including the necessary tissue mounting media. Dr. Michael Angelo will conduct the imaging on the MIBI SIMS.

Work will take place over the full three year grant period, and will progress from development of the multiplexed IHC and multiplexed ISH probes in the initial phases of the project to completing the imaging of the breast cancer validation studies for the complete clinical assays. The validation will occur in two phases also with the 12-plex IHC followed by the 21-plex ISH assays.

Work will involve imaging on average one day per two weeks to obtain the data needed for this project. Therefore, a substantial budget is needed for the MIBI SIMS imaging time.

Initial image data will be processed, as previously described, using software developed in the Nolan lab, but subsequent image quantitation and comparisons to the clinical data will occur at UC Davis.

Impact

This unique technology generates detailed cell-by-cell, highly multiplexed molecular tumor phenotypes and has generated significantly new biological insights which have tremendous clinical potential. For example, spatially resolved evaluation of the activity-state of numerous signaling pathways simultaneously (via phospho-epitope-sensitive antibodies, e.g.) and open chromatin is now possible. Moreover, the ability to detect multiple molecular species within cells and organelles with ~50-nm resolution (anticipated)—in 3D—is revealing completely new vistas in basic and translational cell science.

Specific Aims

Specific Aim 1. Optimize and validate tissue preparation and labeling techniques for multiple (>>10) mass-tagged antibody labeling.
Sub-Aim 1.1. Using formalin-fixed, paraffin-embedded tissue samples, **determine how many protein analytes can be detected simultaneously via mass-tag-labeled antibodies.**
Sub-Aim 1.2. Characterize effects of pre-analytical variables, such as fixation time and archival storage, on antigen-retrieval requirements and detection success. Identify internal analyte controls for sample quality estimation and quantitative normalization.
Sub-Aim 1.3. Validate analytical protein detection results using various metrics, including: linearity; dynamic range; sensitivity (signal-to-noise and signal-to-background); reproducibility; label stability, among others.

Specific Aim 2. Develop or apply software prototypes for **(2.1)** image display, **(2.2)** image segmentation, and **(2.3)** high-dimensional data analytics.
Specific Aim 3. Demonstrate and extend utility of MIBI in a variety of experimental and clinical contexts.
Sub-Aim 3.1. Compare with existing quantitative single and panel-based clinical immunohistochemistry.
Sub-Aim 3.2. Assess drug effects in preclinical models by monitoring multiple pathway phenotypes simultaneously on a cell-by-cell basis.
Sub-Aim 3.3. Define practical resolution limits for detecting multiplexed subcellular protein Distribution - a basic and translational research tool.

Specific Aims 2 and 3 have been addressed by the Angelo and Nolan labs. A brief description is provided and a submitted manuscript that describes the new MIBI-TOF (multiplex ion beam imaging time of flight) instrument and its application to clinical FFPE samples is attached in the **Appendix**.

In previous work we demonstrated a proof-of-principle for multiplexed ion beam imaging (MIBI) 4, a method that utilizes elementally labeled antibodies and secondary ion mass spectrometry (SIMS) to achieve multiplexed imaging with high resolution and sensitivity in archival human tissue biopsies. The SIMS instrument used previously was a Dynamic NanoSIMS 50L Cameca in which the secondary ions are mass separated by a magnetic sector. However, a number of limitations specifically the number of channels (seven) was the motivation to develop a next-generation instrument.

In contrast to the first generation of MIBI instead of a magnetic sector, ion detection is now achieved in static rather than dynamic SIMS with a linear time of flight (TOF) mass spectrometer, where mass is calculated by determining the time it takes for each ion to arrive at a single ion detector relative to a common start time. Since discrete detectors for each mass are not required in static SIMS, the entire elemental mass spectrum thereby is acquired for each pixel in the image. However, linear TOF analyzers common to static SIMS require 20µs or more to acquire a mass spectrum for secondary ions generated by only 10-20ns of sample sputtering. Consequently, ions are being generated for analysis less than 0.1% of the time, making the overall time needed to analyze the same amount of material by static SIMS three orders of magnitude longer over dynamic SIMS.

With this in mind, we sought to design a purpose built mass spectrometer for MIBI analysis that combines a high resolution, continuous primary ion source with orthogonal acceleration TOF detection to achieve subcellular imaging that is both high throughput and highly multiplexed, without compromising sensitivity. The new instrument enables routine, robust imaging of formalin-fixed paraffin-embedded (FFPE) human tissue biopsies with 36x greater throughput than our proof-of-principle work while maintaining sensitivities comparable to magnetic sectors. MIBI-TOF can simultaneously quantify all naturally occurring elements from hydrogen to uranium. We used this capability here to simultaneously quantify 36 elementally labeled antibodies as well as native biological elements such as phosphate and iron. Additionally, we show that MIBITOF allows for repeat scanning of a single section, enabling intelligible study designs at different scales of throughput and resolution, or even acquisition of multiplexed three dimensional images. These properties uniquely position this platform to directly examine numerous questions in the fields of cancer, immunology, and neurobiology in large clinical cohorts.

Significant Instrument improvements

The design of MIBI-TOF focused on highly multiplexed mass detection, increased field of view (FOV) size, and minimized image acquisition times while maintaining high sensitivity. The magnetic sector has been replaced by a TOF (time of flight) analyzer that can now detect 42 metal labeled antibodies simultaneously. Furthermore, MIBI-TOF is capable of sensitive imaging across the elemental spectrum with a quantitative dynamic range of >100,000. A detailed description of the MIBI-TOF instrument specifications are provided in the attached manuscript (Keren et al).

Exemplary imaging data

To assess the capabilities of MIBI-TOF a breast cancer tissue slice was imaged with a 36-antibody panel. Within the same image, we quantified both metal tagged antibodies as well as endogenous elements that varied in abundance by over six orders of magnitude. This combination of high sensitivity, high dynamic range, and low crosstalk permitted us to quantify low abundance markers such as FOXP3 even in the presence of high abundance signals such as double stranded DNA that exceed it in intensity over three orders of magnitude **(Fig.1a, b)**.

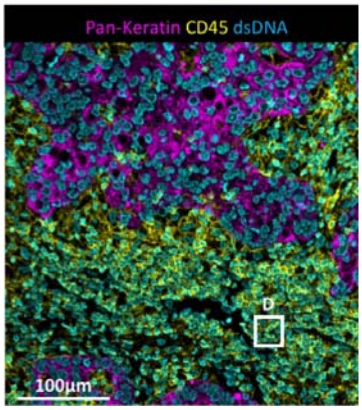

Figure 1a

by
B

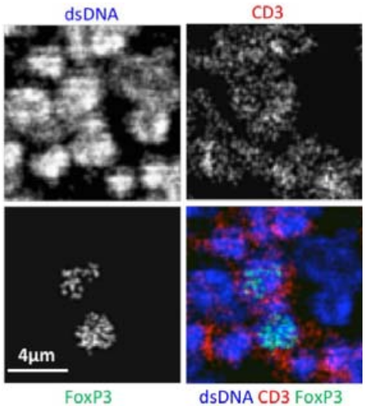

Figure 1b

Figure 1a and b: FFPE human breast carcinoma was stained with a panel of 36 antibodies and a 500x500µm2 field of view was imaged by MIBI-TOF. **1a**: Multiplexed staining for dsDNA, pan-Keratin, and CD45, White box marks inset shown in **1b**. Zoom-in on1a depicting staining for dsDNA, CD3 and FoxP3, ranging over three orders of magnitude in intensity.

Subcellular architecture

Part of our current effort is focused on studying cellular substructure. For this we are exploiting the abundance of naturally occurring isotopes such as ^{12}C, ^{13}C, ^{14}N, ^{15}N, ^{16}O, ^{18}O, ^{31}P, ^{32}S and measuring their cellular distribution. Incorporating measurements of these isotopes with antibodies will provide an unprecedented level of resolution of cellular architecture that will enable models to be built for normal and diseased cells. Although the relevance of this to cancer is clear, this application will be relevant to many other disease states. Below we provide our preliminary experiments looking inside the nucleus, specifically at chromatin structure.

Visualization of open chromatin

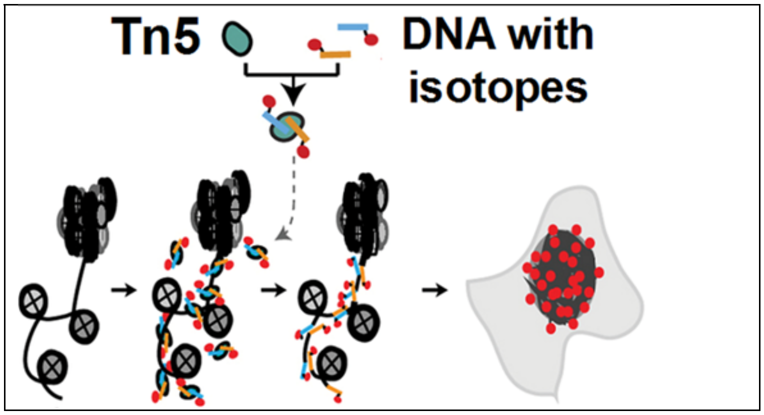

Figure 2: Super-resolution open chromatin imaging.

In a human cell, approximately two meters of DNA are packed within a five-micron nucleus—a topological challenge solved by the cell through the hierarchical folding of DNA around histone proteins to form nucleosomes, and the compaction of nucleosomes into chromatin (Kornberg, 1974). This hierarchical packaging sequesters inactive genomic regions and leaves biologically active regions – be they promoters, enhancers, or other regulatory elements – accessible to transcription machinery. Within the chromatin architecture further transcriptional regulation is imposed by a dynamic epigenetic code that includes DNA methylation, nucleosome positioning, histone composition, and modification, as well as transcription factors, chromatin remodelers, and non-coding RNAs. Together chromatin architecture both physical and chemical (through covalent modification with certain groups) has an essential role in determining the phenotype of a cell. However, in spite of the wealth of knowledge about the complexity of chromatin structure relatively little is known about the overall or genome-wide structure of chromatin, taking into account all the above features. Up until recently methodologies for assaying chromatin structure and composition often required tens to hundreds of millions of cells as input material, averaging out the information from cellular populations. This necessarily missed important information within cellular sub-types that could not be acquired in amounts sufficient for genome-wide chromatin analyses.

The assay of transposase accessible chromatin (Buenrostro et al., 2013) (ATAC-seq) uses hyperactive Tn5 transposase (Tn5) (Goryshin and Reznikoff, 1998; Adey et al., 2010) to simultaneously cut and ligate adapters for high-throughput sequencing at regions of increased accessibility. Genome-wide mapping of insertion ends by high-throughput sequencing allows for multidimensional assays of the regulatory landscape of chromatin. While this assay has provided invaluable information about the chromatin landscape, by its nature it cannot provide details about physical structure. Thus, taking advantage of ATAC-Seq, to visualize open chromatin by inserting fluorescent DNA adaptors into accessible chromatin loci with hyperactive Tn5 transposase we reasoned that by loading Tn5 transposase with fluorine-labeled adaptors instead, the inserts could enable us to image the accessibility of genome at super resolution in 3D. *Taking advantage of the finely focused primary ion beam of nanoSIMS, which allows to imaging of single cells and tissue with sub-cellular resolution (50 nm), here we proposed to investigate the 3D organization of chromatin using super-resolution nanoSIMS imaging.*

As a first step we determined whether ^{31}phosphorus that is the naturally occurring monoisotopic element could be used to visualize DNA. The image below shows permeabilized Jurkat cells that were incubated with a ^{13}C-conjugated antibody against DNA. Using a pseudo coloring scheme of red for ^{13}C-anti DNA and green for ^{31}P followed by a merge we can discern the DNA as yellow thereby validating the approach of using the naturally occurring isotope of phosphorus to visualize DNA **(Figure 3a)**. In the second step of this experiment we visualized open chromatin with fluorine-labeled Tn5 as shown in the merge of **Figure 3b**.

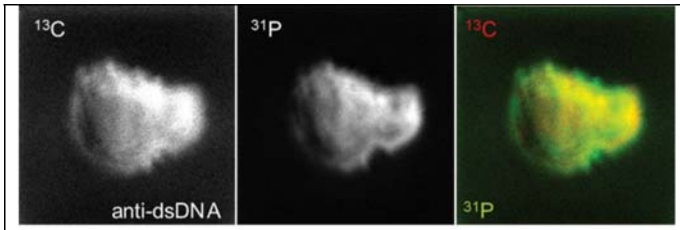

Figure 2a: an antibody to double stranded DNA validates the use of naturally occurring ^{31}P to mark DNA

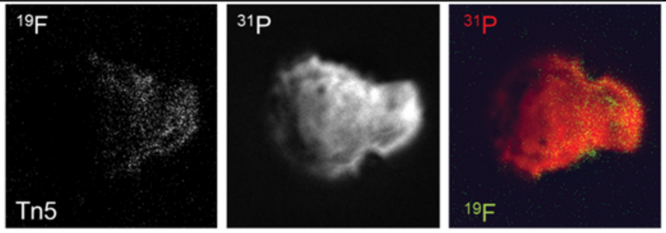

Figure 3b: Fluorine tagged Tn5 and 31P together reveal open chromatin in Jurkat cells.

Visualization of open chromatin

As described in our previous report we are continuing our efforts to optimize the visualization of chromatin structure in single cells. Together chromatin architecture both physical and chemical (through covalent modification with certain groups) has an essential role in determining the phenotype of a cell. However, in spite of the wealth of knowledge about the complexity of chromatin structure relatively little is known about the overall or genome-wide structure of chromatin, taking into account all the above features at high resolution. Up until recently methodologies for assaying chromatin structure and composition often required tens to hundreds of millions of cells as input material, averaging out the information from cellular populations. This necessarily missed important information within cellular sub-types that could not be acquired in amounts sufficient for genome-wide chromatin analyses. The assay of transposase accessible chromatin with high throughput sequencing (Buenrostro et al., 2013) (ATAC-seq) uses hyperactive Tn5 transposase (Tn5) (Goryshin and Reznikoff, 1998; Adey et al., 2010) loaded in vitro with DNA adaptors for high throughput sequencing, that are selectively inserted into accessible chromatin loci within living cells. Deep sequencing of adaptor-tagged sites reveals active regulatory elements, transcription factor binding sites, and nucleosome positions within open chromatin (Buenrostro et al., 2013).

While ATAC-Seq has provided invaluable information about the chromatin landscape, by its nature it cannot provide details about physical structure. In a follow-up study the same group reported a modified version of ATAC-Seq called transposase-accessible chromatin with visualization (ATAC-see), a transposase-mediated imaging technology that directly images the accessible genome *in situ* (Chen et al. Nature Methods 2016). ATAC-see utilizes hyperactive Tn5 transposase loaded with fluorophore-conjugated adaptors to insert into accessible chromatin loci. The fluorophore used was **ATTO 514,** a new hydrophilic fluorescent label with strong absorption, high fluorescence quantum yield, and exceptional thermal and photo-stability. 3D spatial organization of accessible DNA *in situ was visualized by confocal microscopy of the ATTO514 labelled cells.*

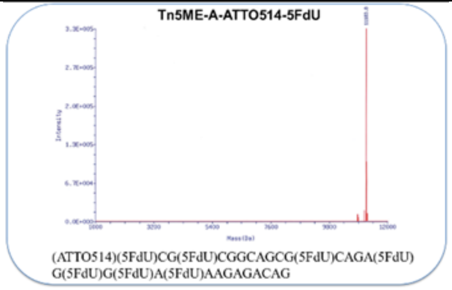

Figure 4A: size and purity of fluorinated adaptors validated by electrospray ionization mass spectrometry

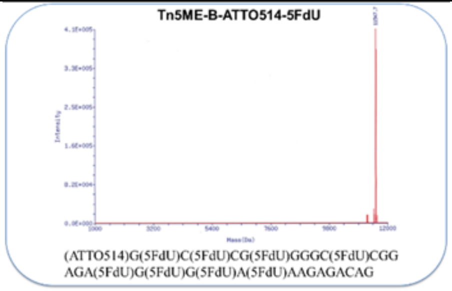

Figure 4b: size and purity of fluorinated adaptors validated by electrospray ionization mass spectrometry

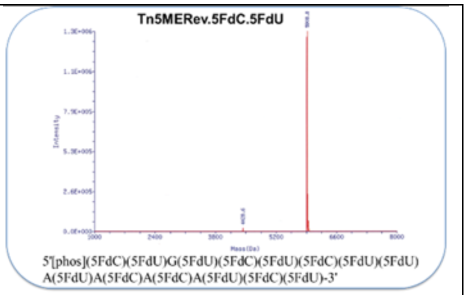

Figure 4c: size and purity of fluorinated adaptors validated by electrospray ionization mass spectrometry

We adapted ATAC-see for MIBI and high resolution nano-SIMS. Using K562 cells as a model system, and taking advantage of ATAC-see to visualize open chromatin by fluorescence, we present a modification of ATAC-see in which fluorinated adaptors conjugated to ATTO 514 loaded onto hyperactive Tn5 transposase can insert into accessible chromatin loci. By endowing these adaptors with a double label (ATTO514 and fluorinated nucleotides with fluorine-modified ribose in the 2' position) open chromatin could be visualized both by florescence and super-resolution nano-SIMS respectively. Below The high purity of the adaptors we used (either singly or doubly labeled) are shown by electron spray ionization mass spectrometry **(Figure 4a - c)**.

Pilot experiments in the K562 cell line with the adaptors shown above **(Figure 5a and b)** demonstrated that ATAC fragment sizes using the recombinant purified hyperactive Tn5 transposase loaded with adaptors conjugated either to both ATTO514 and fluorinated oligos or to only fluorinated oligos generated very similar distributions of insert size **(Figure 2)** and distance from the transcriptional start site (TSS) **(Figure 3)** compared with unmodified Tn5-loaded adaptors. Furthermore, the genomic distribution of ATAC-seq peaks were also similar between Tn5 loaded with Atto514-fluorinated adaptors and Nextera Tn5 (that uses unmodified adaptors) **(Figure 4)**. Thus, ATTO514 and fluorinated tags does not affect Tn5 transposase activity.

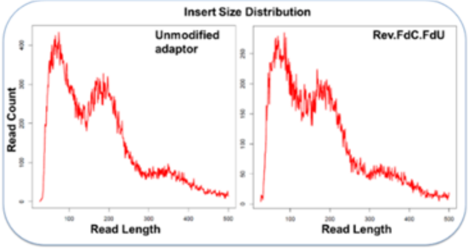

Figure 5a: Tn5-loaded with fluorine- modified adaptors show similar insert size distribution when compared with unmodified Tn5-loaded adaptors. Note the adaptors are double-stranded with the modified adaptor hybridized with a complementary unmodified (reverse (Rev)) strand.

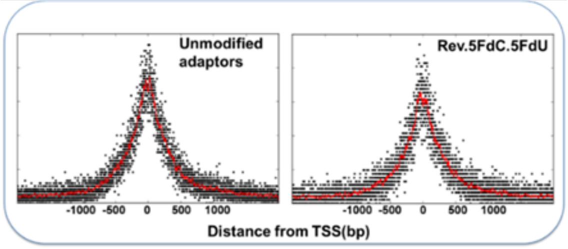

Figure 5b: Tn5-loaded with fluorine-modified adaptors show similar distribution of distances from transcriptional start sites (TSS) when compared with unmodified Tn5-loaded adaptors.

Our modified ATAC-see experiments revealed the 3D spatial organization of accessible DNA *in situ*. After incubation with Tn5 loaded with modified adaptors, the resulting high resolution nano-SIMS images showed that the accessible chromatin is heterogeneously distributed throughout the nucleus (fluorinated signals) and is distinct from endogenous phosphorus which demarcates DNA. Thus, the signal shows the integration of fluorinated adaptors into accessible genomic DNA.

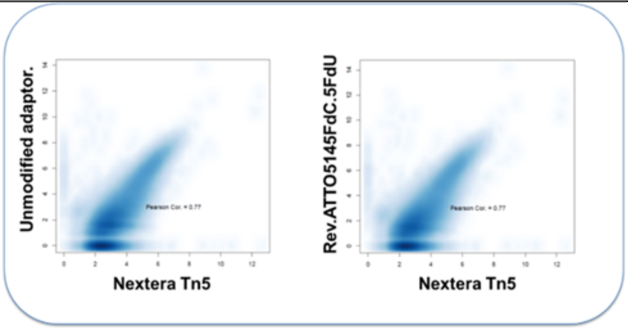

Figure 6: Genomic distribution of ATAC-seq peaks were similar among ATTO 514-fluorinated adaptor loaded Tn5 and Nextera Tn5

Additional technological advances for reagent generation

i) Reasoning that ATTO514 has a similar chemical structure to fluorescein and oregon green we evaluated an antibody that recognizes these fluorophores as also being able to recognize ATTO514. Indeed, we successfully validated an anti-FITC antibody as a reagent to recognize ATTO514. This could be valuable for amplifying the ATAC-see signal further and a new reagent for mass cytometry.

ii) Generation of ^{19}F-trans-activating (tracr)RNA:dCas9 probes. So far, we have generated major satellite (MajSat) sgRNA which recognizes the repetitive sequences found in the pericentromeres. This will provide insight into chromosomal packaging and spindle attachment adding another dimension to the study of nuclear architecture. Since our CRISPR/Cas9 system works well for the visualization of repetitive sequences we can also visualize other nuclear organelles and loci such as, centromere DNA, telomere DNA, ribosomal DNA or Muc4 and Muc1 genes To date, we have visualized pericentromeres, centromeres and telomeres in mouse cells (MEF cells) and telomeres in human cells (Jurkat cells).

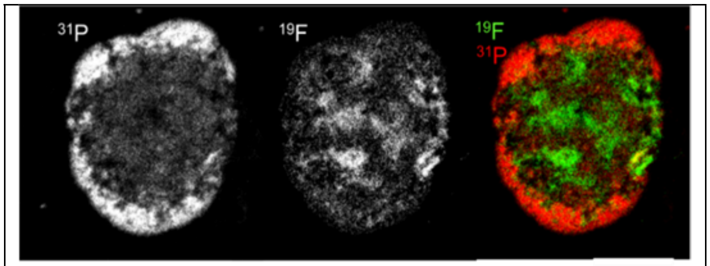

Figure 7: ATTO514-Fluorine-Tn5 (open chromatin) signals inversely correlate with endogenous phosphorus (DNA) as expected.

Generation of halogen-labeled antibodies to further increase the number of parameters to measure per single cell with nanoSIMS or MIBI. We have successfully labelled antibodies with nucleotides synthesized with halogens which can then be a readout for multiplex imaging (Figure 5).

iii) Generation of monoclonal antibodies using "heavy" arginine. By culturing hybridomas in media containing heavy arginine labeled with^{13}C, the resultant antibody will be another reagent for MIBI and nanoSIMS.

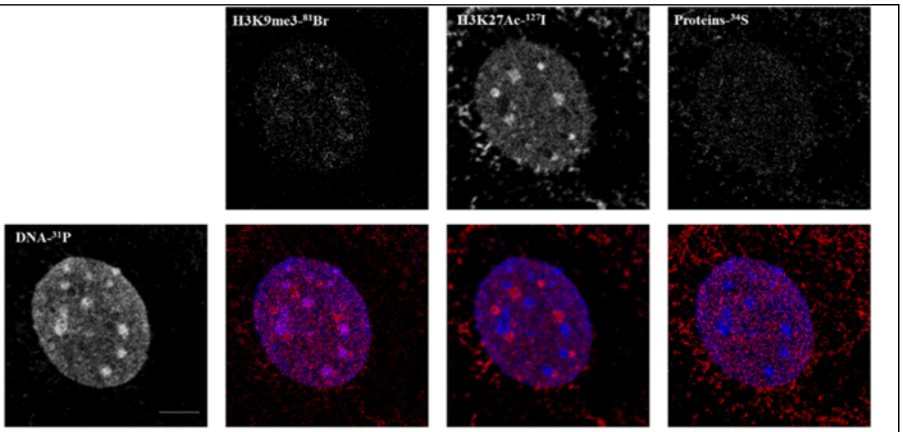

Figure 8: Antibodies conjugated with halogen-labeled oligos can be analyzed by MIBI to reveal chromatin structure.

The tools we have developed now enable us to integrate imaging and epigenomics to provide a general and scalable approach for characterizing the spatio-temoral architecture of gene control under normal and disease conditions.

4. IMPACT

Opportunities for training and professional development This award provided numerous opportunities for training and development of many graduate students, post-doctoral fellows and clinical fellows that were a part of the Nolan group. While the Nolan group benefited as a whole, specific individuals who were funded include: Michael Angelo MD Ph.D, Assistant Professor, Sizun Jiang Ph.D (Post-doc), Julia Kennedy Darling Ph.D (Post-doc) and Christopher Playter, Research Associate who went to graduate school. We also hosted scientists from around the world to spend time in the Nolan Lab and learn about MIBI.

Dissemination of results

Molecular Medicine Tri-Conference 02/2014, San Francisco, CA. *Mass Tags and IHC—A New Frontier for 100 Parameters and Above*

New Technologies Applicable to Study of T-cell lymphomas 02/2014, San Diego, CA

Single Cell Symposia 02/2014, University of Pennsylvania, Philadelphia, PA

American Association of Cancer Researchers (AACR) 03/2014, San Diego, CA

Keynote, Translational Research and Applied Medicine Program 03/2014, Stanford, CA. *A Systems Structured View of Immunity and Cancer*

Cotlove Award Lecture 05/2014, Academy of Clinical Laboratory Physicians & Scientists, San Francisco, CA. *A structure for immunity and cancer at the single level*

Keynote Speaker 05/2014, TRAM Symposia and Retreat, Stanford, CA. *A Systems Structured view of Immunity and Cancer.*

Keynote, MCMi Regulatory Science Symposium 06/2014, Silver Spring, MD

Fluidigm Symposium, 06/2014 Tokyo, Japan

Dana Farber Cancer Center 06/2014, Boston, MA

Nature Conference 06/2014 - Genomic Technologies & Biomaterials for Understanding Disease, San Diego, CA. *A definable “structure” for the immune system and cancers at the single cell level*

The Immune System and Cancer, 09/2014 Banbury Center of Cold Spring Harbor Laboratory, NY. *Single cell proteomics and genomics at high scale*

Translating Imaging and Other Novel Approaches 09/2014, Trinity College, Oxford, UK

Science Day at MedImmune, 10/2014 Mountain View, CA

“Intra-Patient Tumor Heterogeneities: Implications for Targeted Therapy” 10/2014 Stanford Cancer institute

Bill and Melinda Gates Foundation 10/2014 - 2014 Grand Challenges Meeting, Seattle, WA

International Society for Computational Biology 11/2014, San Diego. *High Parameter Single Cell Analysis define a Structured Immune System & Cancer Hierarchies*

Department of Defense OCRP Programmatic Review, 12/2014 Baltimore, MD

Google Stand Up to Cancer (SU2C), 01/2015 Mountain View, CA. *Imaging*

Stanford Medicine Leadership Retreat, 01/2015 Sausalito, CA

AACR: Translation of the Cancer Genome, Cancer Computational & Systems Biology, 02/2015 San Francisco, CA

American Institute for Medical and Biological Engineering, 03/2015 Washington, DC

Institute for Cellular & Molecular Biology, 04/2015 University of Texas, Austin, TX. *A systems structured view of Immunity and Cancer.*

Immunology Forum Seminar 05/2015, Johns Hopkins School of Medicine, Baltimore, MD

Interrogating Complex Biological Systems Symposium, 05/2015 Johns Hopkins Medicine, Baltimore, MD

14th Annual Koch Institute Cancer Research Symposium, 06/2015 MIT, Cambridge, MA

Cold Spring Harbor Labs “Single Cell Analysis Course”, 06/2015 Cold Spring Harbor, NY

Plenary Speaker, 06/2015 FOCIS 2015, San Diego, CA

SU2C - Google[x] Technology and Analysis Satellite Meeting, 07/2015 Boston, MA

Protein Society 29th Annual Symposium, 07/2015 Barcelona, Spain

Tisch Cancer Institute “Frontiers in Oncology" 09/2015 Lecture, New York, NY

Second Edition Systems Biology of Infection Symposium, 09/2015 Zurich, Switzerland

University of California San Francisco Human Immunology, 09/2015 San Francisco, CA

Seminar, 09/2015 Baylor, TX

Sanger Institute, 09/2015 Cambridge, UK

Joint CRI-CIMT-EATI-AACR Meeting, 09/2015 New York, NY

Frontiers in Medicine, 10/2015 Stanford, CA. *A million answers in every cell*

DFCI-Oncology, 10/2015 Boston, MA

Parker Institute for Cancer Immunotherapy, 10/2015 New York, NY

Sino-US Symposium, 10/2015 Stanford, CA

Fluidgm Talk, 10/2015 Berkley, CA

Personalized Medicine World Conference 2016, 01/2016 Mountain View, CA

Big Data to Human Immune Responses, 02/2016 Irvine CA

Realize the Practical Applications of RNA-Seq, 04/2016 San Francisco, CA

Harvard Annual Pathology Retreat, 05/2016 Boston, MA

The American Association of Immunologists, 05/2016 Seattle, WA

Gladstone, 05/2016 San Francisco, CA

Actelion Pharmaceuticals Ltd, 05/2016 Allschwil, Switzerland

Changing Views in Cancer, 06/2016 Charité, Berlin

TxSACT, 06/2016 Houston, TX

GRC, 07/2016 Hong Kong, China

SATU Sympoisum, 07/2016 Taiwan, R.O.C.

Institute of Molecular Biology Academia 07/2016 Sinica, Sinica, Taipei

EarthRise at IONS 09/2016 Petaluma, CA. *The Illusion of Heterogeneity in Cancer*

Stanford Immunology Scientific Conference 09/2016 Stanford, CA. *Organizing the Cancer/Immune System Heterogeneity Illusion with Deep Phenotypic Profiling.*

Amgen 09/2016 San Francisco, CA. *Bringing Order to the Heterogeneity Illusion in Cancer.*

Animal Model Development Workshop 09/2016 Bethesda, MA. *Organizing the Diversity in Blood and Tissue via High Parameter Analysis.*

Medimmune 09/2016 Mountain View, CA. *The Illusion of Heterogeneity in Cancer*

Nature Conference 09/2016 Seattle, WA. *Single cell deep profiling of cancer and immunity.*

Cell Symposia 10/2016 Berkley, CA. *A Defined “Structure” for the Immune System That Reflects Immune Surveillance & Mechanistic Processes.*

Human Cells 10/2016 London, England. *A Defined “Structure” for the Immune System That Reflects Immune Surveillance & Mechanistic Processes.*

AACR 10/16 Boston, MA. *The Illusion of Heterogeneity in Cancer*

University of Pennsylvania, 10/2016 Philadelphia, PA. *A Defined "Structure" for the Immune System That Reflects Immune Surveillance & Mechanistic Processes.*

Parker Institute Retreat 10/2016 Middleburg, VA. Organizing the Cancer/Immune System Heterogeneity Illusion with Deep Phenotypic Profiling

UCSF Pathology Department 11/16 San Francisco, CA. Organizing the Cancer/Immune System Heterogeneity Illusion with Deep Phenotypic Profiling

17th Annual PI Meeting 12/2016 Bethesda, MD. *A Defined "Structure" for the Immune System That Reflects Immune Surveillance & Mechanistic Processes.*

Genome Sciences Seminar UW 01/17 Seattle, WA. *The Heterogeneity Illusion: High Parameter Imaging of Cancer & Immunity.*

Mass Spectrometry: Applications to the Clinical Laboratory 01/2017 Palm Springs, CA. *A Defined "Structure" for the Immune System That Reflects Immune Surveillance & Mechanistic Processes.*

Advances in Genome Biology and Technology – AGBT 02/2017 Ft. Lauderdale, FL. *Sequencers as Flow Cytometers: Ultra-High Throughput Single Cell Analysis of Proteins and RNAs by Split-pool Synthesis.*

Immune Mediated Inflammatory Diseases 02/2017 Wellcome, London, England. *Human immune response monitoring / Deep Immune Phenotyping.*

La Jolla Institute for Allergy and Immunology 03/2017 La Jolla, CA. *A Defined "Structure" for Immune Systems that Reflects Immune Surveillance & Mechanistic Processes.*

Wayne State School of Medicine 03/2017 Detroit, MI. A Defined "Structure" for Immune Systems that Reflects Immune Surveillance & Mechanistic Processes

Keystone 03/2017 Vancouver, BC. A *Defined "Structure" for Immune Systems that Reflects Immune Surveillance & Mechanistic Processes.*

Association of Bimolecular Recourse Facilities – ABRF 03/2017 San Diego, CA. *A Defined "Structure" for Immune Systems that Reflects Immune Surveillance & Mechanistic Processes.*

AACR Annual meeting 04/2017 Washington, DC. *A Defined "Structure" for Immune Systems that Reflects Immune Surveillance & Mechanistic Processes.*

ISB Symposium 04/2017 Seattle, WA. *A Defined "Structure" for Immune Systems that Reflects Immune Surveillance & Mechanistic Processes.*

UT Southwestern 04/2017 Dallas, TX. *A Defined "Structure" for Immune Systems that Reflects Immune Surveillance & Mechanistic Processes.*

MD Anderson 04/2017 Houston, TX. *A Defined "Structure" for Immune Systems that Reflects Immune Surveillance & Mechanistic Processes.*

PICI Institute 04/2017 Santa Barbara, CA. *A Defined "Structure" for Immune Systems that Reflects Immune Surveillance & Mechanistic Processes.*

RNA Seq 2017 04/2017 San Francisco, CA. *A Defined "Structure" for Immune Systems that Reflects Immune Surveillance & Mechanistic Processes.*

National Jewish Health, 05/2017 Denver, CO. *A Defined "Structure" for Immune Systems that Reflects Immune Surveillance & Mechanistic Processes.*

Memorial Sloan Kettering 05/2017 New York, NY. A Defined "Structure" for Immune Systems that Reflects Immune Surveillance & Mechanistic Processes

ASGCT 20th Annual meeting 05/2017 Washington, DC. *A Defined "Structure" for Immune Systems that Reflects Immune Surveillance & Mechanistic Processes.*

Filovirus workshop 05/2017 Rockville, MD. *A Defined "Structure" for Immune Systems that Reflects Immune Surveillance & Mechanistic Processes.*

Keystone 2017 05/2017 Stockholm, Sweden. *A Defined "Structure" for Immune Systems that Reflects Immune Surveillance & Mechanistic Processes*

FOCIS 2017 06/2017 Chicago, IL. A Defined "Structure" for Immune Systems that Reflects Immune Surveillance & Mechanistic Processes

Pezcoller Symposium 06/2017. Trento, IT. *A Defined "Structure" for Immune Systems that Reflects Immune Surveillance & Mechanistic Processes.*

FDA Science Board 06/2017 Silver Spring, MD. *A Defined "Structure" for Immune Systems that Reflects Immune Surveillance & Mechanistic Processes.*

FASEB 07/2017 Snowmass Village, CO. *A Defined "Structure" for Immune Systems that Reflects Immune Surveillance & Mechanistic Processes.*

Technology Transfer

Nothing to report.

Impact on Society Beyond Science and Technology

Nothing to report.

5. CHANGES/PROBLEMS

Nothing to report.

6. PRODUCTS

Jensen, H., S.Y. Chen, L. Folkersen, **G.P. Nolan** and L.L. Lanier, *EBI3 regulates the NK cell response to mouse cytomegalovirus infection.* Proc Natl Acad Sci U S A, 2017. **114**(7): p. 1625-1630.

Mukherjee, S., H. Jensen, W. Stewart, D. Stewart, W.C. Ray, S.Y. Chen, **G.P. Nolan**, L.L. Lanier and J. Das, *In silico modeling identifies CD45 as a regulator of IL-2 synergy in the NKG2D-mediated activation of immature human NK cells.* Sci Signal, 2017. **10**(485).

Gonzalez, V.D., N. Samusik, T.J. Chen, E.S. Savig, N. Aghaeepour, D.A. Quigley, Y.W. Huang, V. Giangarra, **A.D. Borowsky**, N.E. Hubbard, S.Y. Chen, G. Han, A. Ashworth, T.J. Kipps, J.S. Berek, **G.P. Nolan**, and W.J. Fantl, *Commonly Occurring Cell Subsets in High-Grade Serous Ovarian Tumors Identified by Single-Cell Mass Cytometry.* Cell Rep, 2018. **22**(7): p. 1875 1888.

7. PARTICIPANTS

Name: Alexander Borowsky
Project Role: PI
Nearest Person Month: 2
Contribution to Project: Dr. Borowsky oversaw the project at UC Davis and corresponded with the Stanford group. He also served at the diagnostic interpretation pathologist for the project, and primary evaluator of all immunohistochemical assays.

Name: Richard Levenson
Project Role: Co-Investigator
Nearest Person Month: 2
Contribution to Project: Dr. Levenson facilitated image analyses required for quantitation.

Name: Hidetoshi Mori

Project Role: Technician
Nearest Person Month: 25
Contribution to Project: Dr. Mori was responsible for the optimization of over 50 independent antibody reagents for the specific detection of all planned analyses. He developed detailed protocols for all of the assays, and performed all of the quantitative comparisons. Two manuscripts are in progress stemming from this work, and Dr. Mori will be the first author of both.

MIBI-TOF: A multi-modal multiplexed imaging platform for tissue pathology

Leeat Keren[1*], Marc Bosse[1*], Steve Thompson[1], Kausalia Vijayaragavan[1], Erin McCaffrey[1,2], Diana Marquez[1], Roshan Angoshtari[1], Noah Greenwald[1, 3], Harris Fienberg[1], Jennifer Wang[1], Neeraja Kambham[1], Garry Nolan[4], Thomas J. Montine[1], Stephen Galli[1], Robert West[1], Sean C. Bendall[1*], Michael Angelo[1*†]

Understanding tissue structure and function requires tools that quantify the expression of multiple proteins while preserving spatial information. Here, we describe MIBI-TOF (Multiplexed Ion Beam Imaging by Time-Of-Flight), a purpose-built instrument that utilizes bright ion sources and orthogonal time-of-flight mass spectrometry to rapidly image antibodies tagged with metal reporters at sub-cellular resolution in intact formalin-fixed paraffin-embedded (FFPE) human tissue sections. We demonstrate quantitative, full periodic table coverage across a 5-log dynamic range that permits visualization of 36 labeled antibodies simultaneously with histochemical stains and endogenous biological elements. We image fields-of-view up to 800x800μm^2 at resolutions down to 260nm while maintaining sensitivity approaching single molecule detection. Additionally, we show how sample rescanning can be used to dramatically increase throughput or to generate multidimensional 3D data. Given its versatility and sample back compatibility, MIBI-TOF is positioned to leverage existing annotated, archival tissue cohorts to explore emerging questions in cancer, immunology, and neurobiology.

1. Department of Pathology, Stanford University
2. Immunology Program, Stanford University School of Medicine
3. Cancer Biology Program, Stanford University School of Medicine
4. Department of Microbiology and Immunology, Stanford University

* These authors contributed equally to this work

Introduction

Our understanding of complex cellular systems has evolved in lock-step with the development of increasingly sophisticated analytical approaches to interrogate them. In particular, understanding how the phenotype of individual cells relates to the function of the multicellular structures they comprise requires the ability to quantify the spatial distribution of multiple proteins across large regions of intact tissue at subcellular resolution. Until recently, routine laboratory assays could only satisfy one of these two requirements – either measuring expression of one or two proteins in intact specimens[1] or many genes or gene products in cell suspensions from dissociated tissues[2,3]. This disparity between our conceptual understanding of multicellularity and the experimental tools at our disposal has driven recent developments of multiplexed imaging modalities based on cyclic fluorescent staining, sequencing, or the use of mass reporters [4–10]. These innovations have advanced our understanding of how single cell phenotypes relate to global function in solid tissue. However, these approaches have been limited in sensitivity, throughput, and often require specialized sample preparation that limit broader use. Thus, there is an unmet need for a multiplexed imaging modality that is sensitive, robust, high throughput, and back compatible with standard tissue processing techniques.

In previous work we demonstrated a proof-of-principle for multiplexed ion beam imaging (MIBI) [4], a method that utilizes elementally labeled antibodies and secondary ion mass spectrometry (SIMS) to achieve multiplexed imaging with high resolution and sensitivity in archival human tissue biopsies (**Fig. 1A**). Tissue sections are stained with a mixture of antibodies with cognate elemental reporters. SIMS is then used to interrogate the sample using a primary ion beam comprised of atomic ions (i.e. O_2^+) that is focused to a small spot size and rastered across the tissue section. The primary ion beam sputters the elemental reporters and tissue-endogenous elements, releasing secondary ions that are quantified through a mass spectrometer. This ultimately results in a high-dimensional image, depicting the expression of multiple proteins. The imaging resolution and sensitivity of SIMS make it especially suited for tissue imaging. SIMS is among the most sensitive methods known for elemental analysis, where depending on the element of interest, as few as five atoms can be detected [11,12]. Additionally, SIMS can achieve imaging resolutions as low as 10nm, not only exceeding the capabilities of laser ablation mass spectrometry by >100-fold [13], but also the light diffraction limit, thus permitting super-resolution imaging.

The majority of SIMS instruments can be classified into two general categories, dynamic or static. Dynamic SIMS instruments, like the one we have used previously [4] (NanoSIMS 50L, Cameca), continuously sputter the sample with a primary beam that in turn produces a continuous stream of secondary ions [14]. The secondary ions are mass separated by a magnetic sector, where each mass of interest is projected onto a separate ion detector. Continuous sputtering maximizes the rate of sample milling, which in turn minimizes acquisition time for a given amount of material. However, the use of a magnetic sector limits the number of masses that can be detected in parallel to the number of ion detectors. Due to cost and complexity, the number of ion detectors does not exceed seven in any commercial instrument. Moreover, mass calibration, primary and secondary ion optics alignment, and sample loading are often complicated and tedious.

In contrast, instead of a magnetic sector, ion detection in static SIMS instruments is achieved with a linear time of flight (TOF) mass spectrometer, where mass is calculated by determining the time it takes for each ion to arrive at a single ion detector relative to a common start time. Since discrete detectors for each mass are not required in static SIMS, the entire elemental mass spectrum thereby is acquired for each pixel in the image. However, linear TOF analyzers common to static SIMS require 20μs or more to acquire a mass spectrum for secondary ions generated by only 10-20ns of sample sputtering. Consequently, ions are being generated for analysis less than 0.1% of the time, making the overall time needed to analyze the same amount of material by static SIMS three orders of magnitude longer over dynamic SIMS[14,15].

With this in mind, we sought to design a purpose built mass spectrometer for MIBI analysis that combines a high resolution, continuous primary ion source with orthogonal acceleration TOF detection to achieve subcellular imaging that is both high throughput and highly multiplexed, without compromising sensitivity. Here, we describe *MIBI-TOF*, which enables routine, robust imaging of formalin-fixed paraffin-embedded (FFPE) human tissue biopsies with 36x greater throughput than our proof-of-principle work [4] while maintaining sensitivities comparable to magnetic sectors. MIBI-TOF can simultaneously quantify all naturally occurring elements from hydrogen to uranium. We used this capability here to simultaneously quantify 36 elementally labeled antibodies as well as native biological elements such as phosphate and iron. Additionally, we show that MIBI-TOF allows for repeat scanning of a single section, enabling intelligible study designs at different scales of throughput and resolution, or even acquisition of multiplexed three-dimensional images. These properties uniquely position this platform to directly examine numerous questions in the fields of cancer, immunology, and neurobiology in large clinical cohorts.

Results

High-throughput, highly multiplexed tissue imaging

The design of MIBI-TOF focused on highly multiplexed mass detection, increased field of view (FOV) size, and minimized image acquisition times while maintaining high sensitivity. As shown in **Figure 1B**, MIBI-TOF is comprised of several key parts: a sample stage for microscope slides; a primary ion source and column for sputtering the specimen and generating secondary ions; a raster scanner, which sweeps the primary ion beam across the selected FOV in a stepwise pattern; an electrostatic analyzer (ESA), which filters secondary ions with respect to kinetic energy; and an orthogonal acceleration TOF mass spectrometer, which can discriminate and quantify elemental isotope abundance from the continuous introduction of ions. A detailed description of instrument specifications can be found in the **Methods** section.

In order to increase the FOV size and minimize image acquisition times compared to previous demonstrations [4], the primary ion source and column were configured to maximize sample sputtering while maintaining spot sizes suitable for subcellular tissue imaging (spot diameter < 1μm). The larger FOV was achieved by increasing the working distance between the ion source and the sample from 400μm on the NanoSIMS to 15mm on MIBI-TOF. To reduce acquisition times under these conditions without compromising spatial resolution, we increased the current density (primary ion current/spot size) by using an O_2^+ duoplasmatron ion source with 20x higher source brightness with a primary column operating at 30kV acceleration voltage (compared to 16kV shown previously [4]). This allowed us to increase the FOV area by over 60-fold compared with the NanoSIMS [1] (**Fig. 1C,D**) while also increasing the current density 7-fold (at 200nm spot size: MIBI-TOF has a current of 175pA using O_2^+ vs. 25pA using O^- for NanoSIMS, **Fig. 1E**). This configuration reduced the time required to scan a 100μm FOV at 500nm resolution from 17 minutes to 3 minutes (**Fig. 1F,G**). Furthermore, MIBI-TOF can collect data on up to 42 metal labeled antibodies simultaneously, whereas the NanoSIMS can only monitor seven channels at a time [4]. Taken together, these improvements reduce the acquisition time for 42 channels at these settings from 102 minutes by NanoSIMS to 3 minutes by MIBI-TOF, resulting in a 36-fold effective increase in throughput.

In order to acquire full elemental mass spectra from a continuous ion source, we replaced the magnetic sector with an orthogonal acceleration TOF analyzer with a high spectral scan rate (**Fig. 1B,H**). Notably, unlike linear TOF analyzers typically used in static SIMS, orthogonal acceleration dictates the start time of each TOF spectrum independently of the incoming secondary ion flux. Limiting the mass range to 1-240m/z permits a scan rate of 80kHz, such that 30% of all incoming ions at 150m/z (60eV ion energy) are orthogonally accelerated and quantified. Although magnetic sector instruments have high mass resolution and near-absence of tailing of one mass peak into another ($>10{,}000m/\Delta m$, $>10^{-6}$ abundance sensitivity) [16,17], these specifications far exceed what is needed to resolve and quantify nominally spaced elemental ions. Head-to-head comparisons using a molybdenum foil standard demonstrated MIBI-TOF to have sensitivities approaching magnetic sector instruments (MIBI-TOF ion transmission is 32% relative to the NanoSIMS 50L, **Fig. 1I, Fig. S1A**), while still achieving the mass resolution sufficient for an elemental assay ($1088m/\Delta m$ FWHM at 98m/z, 0.4% abundance sensitivity) **Fig. 1J,K, S1A-C**).

Although the TOF here can easily resolve elemental isotopic reporters, delineating them from interfering polyatomic ions with the same nominal mass can be more challenging. To reduce the contribution of interfering polyatomic ions (i.e. organic abducts, oxides and hydrides), we introduced an ESA, which acts as an energy filter on the secondary ions (**Fig. 1B,L**). An extraction field directs the secondary ion flux containing monoatomic and polyatomic ions through the ESA which has been tuned to preferentially transmit mono-atomic ions, which have a larger proportion of high energy species relative to polyatomic ions [18] (**Fig. 1L, S1D**). As a result, ~80% of mono-atomic elemental ions entering the ESA are transmitted to the entrance of the TOF, while the

---

relative abundance of interfering polyatomic ions are attenuated nearly ten-fold (**Fig. S1E**).

Lastly, to increase compatibility with an anatomic pathology workflow, we used an airlock system for loading standard microscope slides that has reduced sample exchange times from 25 min to 3 min (**Fig. 1B**). This, combined with a novel method of conductive gold slide preparation (**Methods**), allows us to utilize conventional techniques for immunohistochemistry (IHC) using FFPE tissue sections (**Fig. S1F**). As a demonstration of this, **Figure 1M** depicts a 500*μ*m FOV multiplexed image of an archival human hippocampus with the hallmark curved dense nuclear band of the dentate gyrus (**Fig. 1M,** arrow), a particularly challenging case for multiplexed fluorescence imaging because of the high levels of autofluorescence arising from the tissue itself. This highly multiplexed subcellular analysis not only captures general neuroanatomical features (dsDNA, EIF4A2, CD289, NCAM/CD56, myelin basic protein (MBP)), but also the identity and location of glial subpopulations (i.e. microglia (IBA1), astrocytes (GFAP)), and specific neuronal (VGLUT2) populations.

Importantly, in addition to charged secondary ions, primary beam rastering also produces secondary electrons that can be visualized with the system's secondary electron detector (SED image, **Fig. 1N**) using primary ion currents that remove negligible amounts of sample. The SED image delineates overall tissue architecture reminiscent of brightfield microscopy and can be used to visualize the sample in real time (Frame rate: 1-4/sec) for direct FOV selection. Using this, hundreds of FOVs can be preselected and subsequently acquired in an automated fashion with no additional input from the user. This allowed a continuous, 24-hour-a-day acquisition for 12 consecutive days showing remarkable stability over time across distinct channels at distinct intensities ($-0.09<R<0.05$, **Fig. 1O**). Altogether, these combination of features reinforce how MIBI-TOF can sensitively and robustly visualize the abundance and subcellular distribution of dozens of proteins simultaneously , and on time-scales enabling large-scale studies.

Sensitive imaging across the elemental spectrum with a quantitative dynamic range of >100,000

In order to benchmark the effective sensitivity for detecting metal tagged antibodies in tissue, we stained human FFPE tonsil sections with 16 different elemental reporter conjugates that were each generated using a single CD45 antibody clone[19,20]. For each section, we compared the number of metal atoms detected by MIBI-TOF per unit area to the absolute values for the same area using solution phase elemental mass spectrometry (**Methods**). The mean ion yield was 0.003, indicating that ~ 1 in every 300 reporter atoms in the tissue sample could be detected, with the most sensitive element (Indium [In]) being ~1:100. Assuming a labeling ratio of 100 reporter atoms per antibody probe using conventional labeling chemistry [20,21] this would permit single-antibody detection in a highly multiplexed platform (**Fig. 2A, Table S1**). **Figure 2A** summarizes the relative sensitivity between elemental metal tags. Significantly, sensitivity of MIBI-TOF far exceeded that of the most sensitive element reported using mass cytometry (CyTOF, ^{159}Tb) by up to 37-

fold depending on the elemental tag used (μ=15, std=9). In these experiments, we also found that the relative yield of elemental adducts (hydrides, oxides, and hydroxides) rarely exceeded 10% of the corresponding elemental signal (μ=5.6%, std=2.8%). A table summarizing elemental adducts can be found in **Figure S1G**.

To assess the capabilities of MIBI-TOF in an applied biological setting, we imaged a breast cancer tissue section stained with 36 antibodies **(Fig. 2B,C)**. Images for the entire 36-plex image are shown in **Figure S2**. **Figure 2B** depicts the mass spectrum, summed over the entire image, at various scales. Within the same image, we were able to quantify both metal tagged antibodies as well as endogenous elements that varied in abundance by over six orders of magnitude. This combination of high sensitivity, high dynamic range, and low crosstalk permitted us to quantify low abundance markers such as FOXP3 even in the presence of high abundance signals such as double stranded DNA that exceed it in intensity by over three orders of magnitude **(Fig. 2C-E)**. To assess detection linearity as a function of ion count rate, a gallium arsenide standard was sputtered with primary ion currents ranging over four orders in magnitude (**Methods**). This demonstrated a linear counting dynamic range exceeding five orders of magnitude before saturating the pulse ion counting system **(Fig. 2F)**. These data illustrate how MIBI-TOF circumvents the analytical limitations of immunofluorescence imposed by channel crosstalk and autofluorescence to permit detection of multiple proteins that vary greatly in abundance, even within the same pixel.

In addition to elemental reporter tags, MIBI-TOF can simultaneously quantify both heavier and lighter elements down to hydrogen. This capability can be used to great effect to quantify elemental components native to the tissue section itself. For example, we quantified ^{12}C and ^{31}P, common elemental components of biomolecules, to obtain images of general tissue structure and nuclear features, respectively (**Fig 2G**). We were also able to detect endogenous metals involved in native biological processes while simultaneously acquiring phenotypic information from a 36-plex antibody staining panel. For example, quantitation of ^{56}Fe in an FFPE spleen section revealed iron stores that co-localized with specific CD68^{+} macrophage subsets with variable amounts of heme oxygenase-1 (HO-1), an enzyme involved in iron porphyrin catabolism [22]. In addition, heavy metal constituents of histopathological counterstains, such as uranyl acetate, can be used to delineate tissue structure in a manner that is independent of protein expression. (**Fig. 2F**). Altogether, these extend the capabilities of MIBI-TOF imaging beyond metal-labeled antibodies.

High dimensional rescanning for customizable tissue pathology workflows

One of the greatest utilities of brightfield microscopy is the ability to revisit the same FOV in a tissue section multiple times at different resolutions. Along these lines, a common approach in anatomic pathology is to first examine a large area at low magnification in order to identify regions of interest to inspect in greater detail at higher magnification. However, virtually all previously reported multiplexed imaging platforms that utilize cyclic fluorescence imaging or laser ablation mass spectrometry can only image a given area once, prohibiting this type of iterative workflow that is commonplace in pathology.

To this end, we designed this platform to function similarly to brightfield microscopy such that the same field can be scanned multiple times. With each scan, secondary ions are released in proportion to the ion dose delivered to the sample per unit area ([primary current] x [acquisition time] / [FOV area]). Since the primary current can be instantly and accurately adjusted across a 10,000x range, a repeatable amount of sample bulk within the same field can be prioritized for rapid low resolution scans using higher primary ion currents or high resolution scans that use lower primary currents [14]. For example, MIBI-TOF imaging of a 200μm FOV of melanoma at 1μm resolution was sufficient to resolve individual nuclei and took only 16 seconds (**Fig. 3A-C**, survey scan, blue). Rescanning of the same field using the same ion dose at 350nm resolution revealed structural features of the nuclear envelope, but increased the acquisition time to 17 minutes (**Fig. 3A-C**, medium res scan, *orange*). Increasing the resolution even further is possible (**Fig. 3A-C**, high res scan, 260nm, *red*), and is accompanied by further increases in scan time.

Scan times at a given resolution scale linearly with FOV area, so an alternative way to reduce acquisition times is to reduce the overall FOV size. For example, a reduction of the FOV size from 200 x 200μm to 100 x 100μm while keeping the resolution fixed reduces acquisition times by 4-fold. Lastly, depending on the abundances of the antigens being detected, the ion dose can be adjusted to ensure a sufficient amount of material is analyzed (**Fig. S3A-B**). Thus, MIBI-TOF can be easily configured for a variety of applications, depending on the number of FOVs, FOV size, protein expression levels and resolution required for each particular study and the time frame available for data collection.

These data highlight an important advantage of ion beam sputtering: the system's sensitivity to metal tagged reporter elements permits generation of robust images for most antigens using a fraction (5-10%) of the total bulk of a standard 4μm thick FFPE section. Thus, high dimensional images can be acquired under conditions that leave much of the sample intact for repeat scanning as described above or for other downstream ancillary studies such as laser capture microdissection [23] (**Fig. 3D**). In **Figure 3E**, a 36-plex survey mosaic image of a full archival breast cancer tissue section (0.8 x 1.04 cm^2) was constructed from 520 separate 400 x 400μm FOVs. The abundance of immune cell subsets demonstrated focal variations in the survey field that correlated with tumor expression of cytokeratin 6 (CK6) and HLA-DR (**Fig. 3F**). Follow-up medium and high-resolution scans of regions of interest (**Fig. 3E**, R1 & R2) containing CK6$^-$ HLA-DR$^+$ tumor cells in the same sample revealed spatially organized immune regulatory populations (**Fig. 3G**). For example, PD-1$^+$ CD4$^+$ T-cells were colocalized with CD8$^+$ T-cells or PD-L1$^+$ macrophages, while B-cells were found to infiltrate the tumor bulk. In contrast, CK6$^+$ HLA-DR$^-$ regions contained relatively few immune cells (**Fig. 3H**). Altogether, this analysis demonstrates how fast, low-resolution scans can guide intelligible selection of regions of interest for subsequent, high-resolution analysis.

Importantly, unlike chromophores and fluorescent molecules, the stable nature of elemental isotopic reporters in archival samples permits valid analysis after extensive periods of time from the initial staining. **Figure 4A** shows serial sections of three breast carcinomas stained on May 2017. The first set of serial sections was analyzed days after staining while the second set was stored at ambient temperature in room air for one year prior to analysis. When comparing the freshly stained and acquired versus stained and aged samples, no deterioration in the quality or quantity of the imaging signal was observed. Altogether, long-term sample stability and rescanning uniquely allows MIBI-TOF to recapitulate routine clinical and research procedures, all while gathering high-dimensional data that permits a detailed view of the tissue.

Reconstruction of Three Dimensional Images from MIBI-TOF Analysis

By leveraging the precision of ion beam sputtering combined with the ability to rescan a field at a fixed resolution, we can also use MIBI-TOF analysis to derive three-dimensional spatial information. Each scan removes the uppermost portion of the tissue to reveal a deeper layer of the tissue bulk that is subsequently analyzed and removed in the following scan. **Figure 4B** illustrates a 15-depth run on an archival 4μm-thick FFPE tissue section of melanoma. Melanoma tumor nuclei (dsDNA, *green*) can be seen becoming more or less prominent in reciprocal fashion with the absence and presence of cytoplasmic (vimentin, *red*) and membranous proteins (Na-K ATPase, *blue*) (**Fig. 4C,** *arrows*; Supp. Movie 1). This type of analysis lays the groundwork for three-dimensional reconstruction of archival tissues and should prove essential for areas of investigation not well suited to planar analysis such as neurobiology and gut immunology.

Discussion

MIBI-TOF is a versatile platform for high-dimensional imaging using standard archival FFPE tissue and conventional IHC workflows. Beyond multiplexing, the imaging analysis is sensitive, automated, and robust with little analytical variability. Up to 42 elemental reporters can be used currently and throughput has been increased by 36-fold over our previous work [4]. In addition to antibody-based approaches, elemental labeling of nucleic acid derivatives should extend the platform to DNA and RNA *in situ* hybridization (ISH). Given that the feasibility of adapting fluorescence-based ISH probes to elemental reporter assays has been demonstrated previously [24,25], we expect to implement these capabilities in the near future, allowing for single cell quantitation of both genomic copy number variants (CNVs) and transcript enumeration within a native histological context.

With a mass range of 1-240m/z, MIBI-TOF can also quantify numerous endogenous elements including carbon, phosphorous, iron, and calcium. The spatial distribution of endogenous biological elements can be used for cellular segmentation, to relate the abundance of enzyme-coordinated metal cofactors to single cell phenotypes, or to assist in identifying abnormal regions of tissue, such as necrosis or fibrosis. Notably, we are working to extend MIBI-TOF to simultaneously detect ^{2}H and ^{13}C heavy isotope reporters which can be used to covalently label the protein or DNA of cells expanded *ex vivo*. Because these isotope reporters are relatively inert, this capability is particularly applicable to ongoing clinical trials using engineered T-cell therapies, allowing for the assessment of how transplanted cell phenotypes evolve over time.

The future of MIBI-TOF applications will be further accelerated as brighter primary ion sources are implemented with up to 20 times the current density as those used here. These improvements should reduce acquisition times proportionally, such that sample throughput would be rapid enough to permit turnaround times compatible with routine anatomic pathology. Additionally, the higher milling rates achieved with these ion sources will also permit rapid depth profiling of large samples, such that high-throughput 3D rendering of tissue architecture would be feasible on a large scale. Full utilization of these capabilities will require development of purpose built computational tools for image segmentation, annotation, visualization, and feature extraction, which we expect to be an important avenue of future research. Along with deployment of the necessary instrumentation, we are working to implement and distribute our initial versions of these tools to enable broader use of MIBI-TOF by clinical and basic research scientists. Altogether, MIBI-TOF represents a robust tool to help overcome long-lasting analytical challenges in systems biology. We believe this platform will play a key role in many important discoveries in cancer biology, immunology, neuropathology, and beyond.

Materials and Methods

MIBI-TOF Tissue Analyzer

The MIBI-TOF tissue analyzer is a dynamic SIMS instrument with orthogonal time of flight ion detection (**Fig. 1B**). The instrument is equipped with a duoplasmatron O_2^+ ion source coupled to a 30kV primary ion column (IOG 30D, Ionoptika, Eastleigh, UK) operating in crossover mode at a working distance of 15 mm and 45° incident angle to the sample stage. The primary column is a conventional two lens design, where the first lens (L1) demagnifies the virtual source and the second lens (L2) functions as a probe forming objective. Depending on the acquisition time and image resolution desired for a specific experiment, L1 voltages of 17-26KV are used to achieve primary current and spot sizes of 18nA and 1um to 240pA and 230nm, respectively. Tissue sections are loaded into the vacuum chamber using a custom designed sample carrier that can accommodate two standard microscope slides. Sample loading times are approximately 3 min while the analysis chamber typically reaches its operational base pressure of $5\text{x}10^{-7}$ within 6 min. Course navigation of tissue sections is achieved via a point and click interface using a co-registered photo of the sample stage. Final field of view selection is performed using a secondary electron detector (SED 03, Ionoptika, Eastleigh, UK) which allows real time imaging of the sample surface as the primary ion source rasters the sample using a primary ion current between 500pA-1nA. Lateral stage coordinates for each field of view specified by the user are tabulated in the acquisition software and imaging run parameters are specified. Prior to starting each run, the primary ion imaging system is focused on a test region of the sample of interest by adjusting the L2 voltage while imaging in real-time

SED mode. A stigmator octopole within the primary ion column is also adjusted to minimize discernable astigmatism. A description of key acquisition parameters and their adjustable ranges of values are listed below:

- Primary ion current: 1pA-1μA
- FOV size: 10 x 10μm – 1 x 1mm
- Pixel dwell time: > 100μs
- Number of pixels: 128x128 to 2048x2048
- Number of depths: 1 or more
- Mass range: Up to 240m/z

Specific settings for each experiment are denoted in **Table S2**. For each pixel in the image, corresponding positions on the tissue are sequentially sputtered with the primary ion beam using a fly back raster pattern (IGM 300, Ionoptika, Eastleigh, UK). Secondary ions are collected using a relatively modest extraction field of approximately 60V/mm, which yields an optical gate of approximately 800μm without the use of dynamic emittance matching (DEM). Secondary ions subsequently pass through a 90^o electrostatic analyzer (ESA) with 5eV energy acceptance that has been tuned for preferential transmission of monoatomic (elemental) ions relative to polyatomic organic species. The ions then enter an orthogonal time of flight mass spectrometer with a median energy acceptance of 65eV, mass range of 1-240m/z, and mass resolution of 1088 m/Δm (FWHM at 98m/z) operating at 80KHz repetition rate (**Fig. S1**). Under these conditions, the predicted TOF transmission of ions with 60eV median energy and 150 m/z is 30%. A discrete dynode ion detector (MagneTOF, ETP Electron Multipliers, Ringwood, Victoria, Australia) with 400ps FWHM pulse width is used for ion detection. The detector output signal passes through a preamplifier stage (ZX60-P103LN+, MiniCircuits Brooklyn, NY) prior to a PCIE time to digital converter with 500ps time resolution (TimeTagger4-2G, Cronologic). A start trigger synchronized with the pushout initiates acquisition with 500ps time sampling across the time interval sufficient to capture 1-240m/z (12μs). Multiple TOF spectra recorded for each pixel are summed and saved to a data file using a modified version of MiniSIMS v2.0.14 (Scientific Analysis Instruments, Manchester UK), which is also used for stage control. A Dell Precision 5000 series desktop computer (Xenon E5-1650 3.5GHz, 32GB 2133MHz DDR4, 512GB SATA3 SSD) running Windows 7 enterprise was used. System sensitivity is assessed over time by measuring the count rate of ^{98}Mo per nA of primary ion current using a pre-sputtered region of molybdenum foil (Ted Pella, Redding California). Initial design and prototype construction of the sample load lock, analysis chamber, secondary ion optics, and TOF were done in collaboration with Scientific Analysis Instruments, Manchester UK. Current commercial MIBI-TOF instrumentation is being manufactured by IonPath Inc., Menlo Park, CA.

Gold Slide preparation

Superfrost plus glass slides (Electron Microscopy Sciences, Hatfield, PA) were soaked in water with 0.1% SDS and rinsed extensively with distilled water and then acetone (Avantor-Macron Fine Chemicals, Center Valley, PA). Acetone was immediately evaporated under a stream of air to avoid trace of residues. Slides were coated with Tantalum (Ta, 30nm coating) and Gold (Au, 100nm). The slides were placed ten at a time in adjustable rails in an e-beam evaporation station and pumped down for about two hours prior to deposition. The base pressure before the deposition was ~4 x 10^{-7} Torr. The distance between the source and the substrate was 30cm. The Ta was evaporated at a rate of ~1nm per second. The Au was evaporated immediately after at a rate of 10-15 Angstroms per second. Gold-coated slides were silanized in acetone with 3-aminopropyltriethoxysilane for 30min then washed with acetone and air dried (Vactabond, Burlingame, CA). Slide were baked at 70˚C for 30 min and kept dry at room temperature until use.

Antibody conjugation

A summary of antibodies, reporter isotopes, and concentrations are described for each experiment in Table S3. Metal-conjugated primary antibodies were prepared as described previously [20]. Following labeling, antibodies were diluted in Candor PBS Antibody Stabilization solution (Candor Bioscience GmbH, Wangen, Germany) to 0.2mg mL^{-1} and stored long-term at 4°C.

Staining

Tissue sections (4µm thick) were cut from FFPE tissue blocks using a microtome, mounted on silanized-gold slides for MIBI analysis. Slide-tissue sections were baked at 70˚C for 20min. Tissue sections were deparaffinized with 3 washes of fresh-xylene. Tissue sections were then rehydrated with successive washes of ethanol 100% (2x), 95% (2x), 80% (1x), 70% (1x), and distilled water. Washes were performed using a Leica ST4020 Linear Stainer (Leica Biosystems, Wetzlar, Germany) programmed to 3 dips per wash for 30 sec each. The sections were then immersed in epitope retrieval buffer (Target Retrieval Solution, pH 9, DAKO Agilent, Santa Clara, CA) and incubated at 97˚C for 40 min and cooled down to 65˚C using Lab vision PT module (Thermofisher Scientific, Waltham, MA). Slides were washed with a wash buffer made with PBS IHC Tween buffer (Cell Marque, Rocklin, CA) containing 0.1% (w/v) BSA (Thermofisher Scientific, Waltham, MA). Endogenous avidin, biotin binding proteins were blocked using Avidin/Biotin blocking systems (Biolegend, San Diego, CA). Sections were treated successively with avidin and biotin blocking solutions for 10 min and washed for 5 min in wash buffer. Sections were then blocked for 1h with 3% (v/v) donkey serum (Sigma-Aldrich, St Louis, MO) diluted in TBS IHC wash buffer (Cell Marque, Rocklin, CA). Metal-conjugated antibody mix was prepared in 3% (v/v) donkey serum TBS IHC wash buffer and filtered using centrifugal filter, 0.1μm PVDF membrane (Ultrafree-MC, Merck Millipore, Tullagreen Carrigtowhill, Ireland). All experiments were stained using two antibody mixes. The first antibody mix was incubated overnight at 4˚C in humid chamber. The second mix contained antibodies of structural genes with strong signal and an anti-biotin antibody. After overnight incubation, slides were washed on an orbital shaker for 5 min in wash buffer. The second antibody mix was then applied and incubated for 1h at 4˚C. Slides were then washed twice for 5 min in wash buffer and fixed for 5min in a 2% diluted glutaraldehyde solution 2% (Electron Microscopy Sciences, Hatfield, PA) in low-barium PBS. Slides were rinsed briefly in low-barium PBS. Tissue sections were dehydrated with successive washes of Tris 0.1 M (pH 8.5), (3x), distilled water (2x), and ethanol 70% (1x), 80%(1x), 95% (2x), and 100% (2x). Slides were immediately dried in a vacuum chamber for at least 1 h prior to imaging. In some experiments, tissue sections were counterstained with 1x Hematoxylin Harris solution (Sigma) or 0.4% uranyl acetate (Electron Microscopy Sciences, Hatfield, PA) for 1 min and rinsed briefly in deionized water. Tissue sections were dehydrated with successive washes of Tris 0.1 M (pH 8.5), (3x), distilled water (2x), and ethanol 70% (1x), 80%(1x), 95% (2x), and 100% (2x). Slides were immediately dried in a vacuum chamber for at least 1 h prior to imaging.

Sensitivity measurements using CD45 conjugates

Anti-human CD45 (CST clone D9M8I) was conjugated to one isotope from each of the metals routinely used in MIBI-TOF experiments (**Table S1**), and each conjugate was used to stain serial sections of human FFPE tonsil sections as described above. From each section, a 100μm FOV was imaged by MIBI-TOF. A total of 40 depths was acquired to ensure that the entire depth of the tissue was scanned. Following imaging, the remaining tissue was dissolved in a low volume of 10% trace metal grade nitric acid. Extracted samples were volume normalized with 1% trace metal grade nitric acid with an equal volume of tuning solution (Fluidigm Sciences) added as an internal standard with an addition of 20nM trace metal grade YCl_3 (Sigma). Samples were run in solution on a CyTOF 2 mass cytometer (Fluidigm Sciences) and the tissue extracted elemental isotope concentration was calculated against a blank sample using an ^{89}Y plus tuning solution standard curve generated at the same time. The total number of reporter atoms in the sample were then calculated based on the volume of the tissue extracted solution. Sensitivity was calculated by comparing the total number of counts detected by MIBI-TOF and the absolute solution quantification, normalized to the tissue area used for both measurements. The number of antibodies needed for detection was calculated under the assumption of ~100 metal atoms per antibody [21].

GaAs measurements

Gallium arsenide (GaAs) semiconductor wafer (Silicon Valley Microelectronics) was cleaved and mounted on a gold slide using double sided carbon tape (Ted Pella, Inc). A 300μm FOV of GaAs was pre-sputtered for 5min using a primary current of 500nA. All primary current measurements were performed via Faraday cup (FC). Accurate current measurements by FC can be performed as low as 1-2pA. However, with the instrument tuned for maximum ion transmission, the count rate of gallium exceeds the capacity of the counting system (100Kcps) using only 100pA. With this in mind, the secondary ion optics were tuned to attenuate the total ion flux entering the TOF such that the gallium count rate remained within the linear range of the counting system when using primary beam currents across a four log range (4pA-46nA). Acquisition times for each primary current value are listed below:

- 930pA-45nA: 65s
- 396pA: 3m 17s
- 44pA: 8m 44s

- 4pA: 32m 50s

Sensitivity comparison between NanoSIMS and MIBI-TOF

To compare the sensitivity of MIBI-TOF and NanoSIMS 50L, the ion count rate for ^{98}Mo was quantified using a molybdenum foil standard (Ted Pella). For NanoSIMS measurements, a 100μm FOV was pre-sputtered for 10 min using 2nA O^- primary ion current. In order to maximize ion transmission and thus sensitivity, entrance slit ES0 was used. The ion count rate at 98m/z were measured using 200pA primary ion current. For MIBI-TOF, a 200μm FOV was pre-sputtered for 1 min using 20nA O_2^+. The ESA was tuned for maximal ion transmission using a voltage gap of 262V. The ion count rate at 98m/z was subsequently measured using 50pA primary ion current.

Acknowledgements

The authors would like to thank David Kirkwood and Paul Blenkinsopp for their expertise and technical support in developing this instrument. Slide preparation was performed at the Stanford Nano Shared Facility (SNSF), supported by the National Science Foundation, under award ECCS-1542152. The authors thank Tom Carver, from the Microfab Shop of SNSF for helpful technical advice and for the thin film evaporation services. The authors thank Tyler Risom, David Glass, and Shirley Greenbaum for discussions and comments. L.K. is a Damon Runyon Fellow supported by the Damon Runyon Cancer Research Foundation (DRG-2292-17) and a non-stipendiary awardee of the EMBO Long-Term fellowship (ALTF 1128-2016). E.F.M is supported by the National Science Foundation Graduate Research Fellowship (Grant No. 2017242837). G.P.N. is supported by grant W81XWH-14-1-0180 from the DoD. R.W is supported by NIH 5R01CA18390402. S.C.B. is supported by a gift from Christy and Bill Neidig, the Damon Runyon Cancer Research Foundation (DRG-2017-09), the NIH 1DP2OD022550, 1-R00-GM104148, 5U19AI116484, and U19 AI104209. M.A is supported by 1-DP5-OD019822. S.C.B, M.A., and T.J.M. are jointly supported by 1R01AG056287 and 1R01AG057915, S.C.B. and M.A. are jointly supported by 1U24CA224309, the Bill and Melinda Gates Foundation, and a Translational Research Award from the Stanford Cancer Institute. S.J.G. is supported by U19 AI104209, R01 AR067145 and R01 AI32494. M.A. and S.C.B. are board members and shareholders in Ionpath Inc. G.P.N is a shareholder in IonPath Inc. H.F. is a shareholder and employee of Ionpath Inc.

Figure legends

Figure 1: MIBI-TOF is designed for high-throughput, highly multiplexed tissue imaging

(A) MIBI-TOF experimental procedure. A tissue section is stained with a mix of antibodies, each labeled with a unique metal isotope. To detect the isotopes, the tissue is rastered, pixel by pixel, by primary charged ions. Secondary ions, released from the tissue, are measured by time of flight mass spectrometry (TOF-MS), to generate an N-dimensional image. **(B)** MIBI-TOF instrumentation. MIBI-TOF is comprised of several key parts: the sample stage, where slides are loaded into the instrument; a primary ion source, which shoots charged particles at the specimen, releasing secondary ions; an electrostatic analyzer (ESA), which filters secondary ions; a TOF mass spectrometer, which measures element abundance; and a raster scanner, which rasters the primary ion beam across the selected FOV in a stepwise pattern. **(C)** An 800x800μm^2 FOV of breast carcinoma imaged by MIBI-TOF. Inset depicts a 100x100μm^2 region, which can be imaged by the NanoSIMS 50L. **(D-J)** Comparison of various parameters for the NanoSIMS 50L and MIBI-TOF. Purple indicates more favorable values. **(D)** FOV sizes **(E)** Current density (current per spot size) **(F)** 100x100μm^2 FOVs were stained and visualized by NanoSIMS (top, 17 minutes) and MIBI-TOF (bottom, 3 minutes). Counterstain for the top image was hematoxylin, and for the bottom was carbon. **(G)** Scan times for the FOVs shown in (F). **(H)** Schematic depicting the mass range (x-axis) measured by NanoSIMS and MIBI-TOF. Whereas the NanoSIMS uses a magnetic sector that inherently limits the number of detectable masses to the number of detectors (<7), MIBI-TOF acquires the entire spectrum from 1-240m/z. **(I)** Sensitivity, measured by scanning a molybdenum standard. **(J)** Mass resolution (mass divided by full width of the peak at half mass). **(K)** FFPE human hippocampus was stained with a panel of 40 antibodies and a 500x500μm^2 FOV of was imaged by MIBI-TOF. Shown is the mass spectrum in the range of 165-175m/z, summed over the entire image. **(L)** Energy filtering by MIBI-TOF. The primary ion beam hits the sample, releasing both elemental isotopes and polyatomic adducts, which may overlap in mass. Polyatomics are energy filtered by the ESA, which prevents them from entering the TOF. Einzel lenses in the secondary ion optics are omitted for clarity. **(M)** Multiplexed staining for dsDNA, VGLUT2, CD298, GFAP, EIF4A2, IBA1 and MBP, corresponding to the spectrum in (K). **(N)** A 200x200μm^2 FOV of human GI tract was stained with a 20-plex panel and scanned with MIBI-TOF. Left: Secondary Electron Density (SED) image. Middle: Antibody staining for dsDNA (blue), Epcam (green) and Vimentin (red). Right: Overlay of antibody stains with SED image. **(O)** A tissue microarray of biopsies from 41 triple-negative breast cancer patients were stained with a panel of 36 antibodies. 800x800μm^2 FOVs were measured continuously, 24-hours a day for 12 consecutive days, with no tuning of the machine. Left: For each biopsy, shown are the intensities, summed over the entire FOV, for dsDNA, beta-catenin and CD56 as a function of acquisition time. Right: Shown is the staining for dsDNA for a 150x150μm^2 inset for the first and last patients measured.

Figure 2: MIBI-TOF can sensitively image across the elemental spectrum with a quantitative dynamic range of >100,000

(A) Human FFPE tonsil sections were stained with a single CD45 antibody clone conjugated to 16 different elemental reporters and the amount of metal detected by MIBI-TOF was assessed by comparing to values attained using normalized, solution phase ICP-MS. For each element shown are the number of antibodies needed for detection (assuming ~100 metals/antibody). The corresponding number is displayed for ^{159}Tb, the most sensitive channel on CyTOF, which is on average 15-fold less sensitive. **(B-C)** FFPE human breast carcinoma was stained with a panel of 36 antibodies and a 500x500μm^2 FOV was imaged by MIBI-TOF. (B) The mass spectrum, summed over the entire image, at various scales. (C) Multiplexed staining for dsDNA, pan-Keratin, and CD45, corresponding to the spectrum in (B). White box marks inset shown in D. **(D)** Zoom-in on (C), depicting staining for dsDNA, CD3 and FoxP3, ranging over three orders of magnitude in intensity. **(E)** For all channels, shown are their intensities, summed over all pixels in the image from (C), over five orders of magnitude. **(F)** Measurements of counts per second for a gallium arsenate probe (y-axis) for a range of extraction currents (x-axis). Red boxes denote limits of linear range, which spans five orders of magnitude. Inset: Gallium isotopic ratio (^{69}Ga/^{71}Ga) measured by MIBI-TOF (black) matches the known ratio (1.5, red) and is constant over three orders of magnitude before saturating the counts system. **(G)** Tissue sections from tonsil (left), spleen (center) and GI (right) depicting simultaneous measurements of natural elements (^{12}C, ^{31}P, ^{56}Fe), metal-tagged antibodies (CD20, dsDNA, CD68, HO1, Epcam) and counterstains (Uranyl-acetate). Arrows denote CD68^{+} HO1^{+} macrophages with high ^{56}Fe.

Figure 3: MIBI-TOF enables multi-scale, high dimensional rescanning for customizable tissue pathology workflows

(A) A 200x200μm^2 melanoma biopsy (inset) was scanned four times at resolutions ranging from 260-1000nm (y-axis). Shown are the scan times for the different resolutions (x-axis). **(B)** Zoom-in on the inset in (A), showing staining for dsDNA (top) or lamin A/C (bottom) for the survey scan (left) and high-resolution scan (right). (C) Zoom-in on the inset in (B), showing staining for dsDNA (top) or lamin A/C (center) and their overlay (bottom) for the different scans. Increasing detail of lamin A/C becomes available at higher resolutions. **(D)** Diagram of microscope-like analytical workflow, enabled by MIBI-TOF. **(E)** Archival breast cancer tissue section was stained with 36 antibodies and a 0.8x1.04cm^2 FOV was visualized using MIBI-TOF. The full image was constructed from 520 400*μ*m fields of view, tiled 26x20. White squares indicate regions depicted in F-H. **(F)** Zoom-in on the regions shown in (E), showing the staining for pan-keratin, cytokeratin 6 (CK6), CD45 and HLA-DR. **(G,H)** R1 and R2 regions from (E) were rescanned at medium (500nm) resolution. Top-left image depicts the entire region. Surrounding images highlight expression of distinct markers in specific regions.

Figure 4: Reconstruction of Three Dimensional Images from MIBI-TOF Analysis

(A) Three FFPE breast carcinomas were stained with a 36-plex panel in May 2017 and 1mm cores were visualized by MIBI-TOF days after staining (insets), or a year later (large images), with negligible deterioration in signal. **(B)** 3D reconstruction of a 15-layer depth profile of archival 4μm-thick FFPE Melanoma tissue stained with a 20-plex panel. **(C)** Snapshots of selected depths. White and yellow arrows denote nuclei (dsDNA, green) that either appear or disappear respectively with depth; with corresponding disappearance or appearance of cytosol (vimentin, red) and membrane (Na-K ATPase, blue).

Supplementary figure legends

Figure S1: MIBI-TOF is structurally designed for high-throughput highly multiplexed imaging with high sensitivity and low noise

(A) Mass spectrum between 91-101 m/z measured for a Molybdenum probe. Dashed box highlights ^{98}Mo, with an abundance sensitivity of 0.4%. **(B)** Isotopic ratios of a molybdenum standard, as expected from the literature (light gray bars) and measured using MIBI-TOF (dark gray bars). **(C)** Zoom-in on ^{98}Mo from (A). FWHM = Full Width at Half Max. **(D)** Serial sections of human tonsil were stained with CD45 ^{147}Sm and imaged by MIBI-TOF. Signal and noise, resulting from organic adducts, (y-axis) are shown for triplicate measurements, in varying ΔV settings (x-axis). Red rectangle indicates setting used for subsequent analysis. **(E)** FFPE human tonsil was stained with CD45 conjugated to ^{147}Sm. Shown are the spectra, summed over all pixels in the image, for two 100μm FOVs, either with (bottom) or without (top) energy filtering. **(F)** Human hippocampus FFPE section on gold slide. Highlighted white square represents the region of interest (ROI) imaged by MIBI-TOF and shown in figure 1M. Gray squares indicate additional areas visualized by MIBI-TOF. **(G)** Human tonsils were stained with CD45 conjugated to different elements and imaged by MIBI-TOF. For each mass, typically used in a MIBI-TOF experiment, shown are the adducts for H,O and OH as a fraction of the intensity of the labeled channel.

Figure S2: 36-plex staining using MIBI-TOF

Shown are images from one MIBI-TOF run of a 400μm FOV of human breast carcinoma.

Figure S3: MIBI-TOF allows to customize ion dose/area to detect antigens with varying abundances

(A) Human breast carcinoma was stained with a panel of 36 antibodies and visualized by MIBI-TOF. Shown are the cumulative counts for a high, medium and low abundant antigen (dsDNA, CD8 and CD4, respectively) for the insets, shown in (B) (y-axis) as a function of increasing ion dose/area (x-axis). **(B)** Images showing dsDNA, CD8 and CD4 signal as a function of increasing ion doses. Arrows point to cells highlighted in insets.

References

1. Matos, L. L. de, Trufelli, D. C., de Matos, M. G. L. & da Silva Pinhal, M. A. Immunohistochemistry as an important tool in biomarkers detection and clinical practice. *Biomark. Insights* **5,** 9–20 (2010).
2. Tirosh, I. *et al.* Dissecting the multicellular ecosystem of metastatic melanoma by single-cell RNA-seq. *Science (80-.).* **352,** (2016).
3. Chevrier, S. *et al.* An Immune Atlas of Clear Cell Renal Cell Carcinoma. *Cell* **169,** 736–749.e18 (2017).
4. Angelo, M. *et al.* Multiplexed ion beam imaging of human breast tumors. *Nat. Med.* **20,** 436–42 (2014).
5. Giesen, C. *et al.* Highly multiplexed imaging of tumor tissues with subcellular resolution by mass cytometry. *Nat. Methods* **11,** 417–422 (2014).
6. Chen, K. H., Boettiger, A. N., Moffitt, J. R., Wang, S. & Zhuang, X. Spatially resolved, highly multiplexed RNA profiling in single cells. *Science (80-.).* **348,** aaa6090-aaa6090 (2015).
7. Coskun, A. F. & Cai, L. Dense transcript profiling in single cells by image correlation decoding. *Nat. Methods* **13,** 657–660 (2016).
8. Huang, W., Hennrick, K. & Drew, S. A colorful future of quantitative pathology: validation of Vectra technology using chromogenic multiplexed immunohistochemistry and prostate tissue microarrays. *Hum. Pathol.* **44,** 29–38 (2013).
9. Stack, E. C., Wang, C., Roman, K. A. & Hoyt, C. C. Multiplexed immunohistochemistry, imaging, and quantitation: A review, with an assessment of Tyramide signal amplification, multispectral imaging and multiplex analysis. *Methods* **70,** 46–58 (2014).
10. Lee, J. H. *et al.* Highly Multiplexed Subcellular RNA Sequencing in Situ. *Science (80-.).* **343,** 1360–1363 (2014).
11. Hervig, R. L. *et al.* Useful ion yields for Cameca IMS 3f and 6f SIMS: Limits on quantitative analysis. *Chem. Geol.* **227,** 83–99 (2006).
12. Wilson, R. G. SIMS quantification in Si, GaAs, and diamond - an update. *Int. J. Mass Spectrom. Ion Process.* **143,** 43–49 (1995).
13. Wirtz, T. *et al.* Towards secondary ion mass spectrometry on the helium ion microscope: An experimental and simulation based feasibility study with He $^+$ and Ne $^+$ bombardment. *Appl. Phys. Lett.* **101,** 041601 (2012).
14. Wilson, R. G., Stevie, F. A. & Magee, C. W. *Secondary ion mass spectrometry : a practical handbook for depth profiling and bulk impurity analysis*. (Wiley, 1989).
15. Vickerman, J. C. & Briggs, D. (David). *TOF-SIMS : materials analysis by mass spectrometry*.

16. Lechene, C. *et al.* High-resolution quantitative imaging of mammalian and bacterial cells using stable isotope mass spectrometry. *J. Biol.* **5,** 20 (2006).
17. Zhang, D.-S. *et al.* Multi-isotope imaging mass spectrometry reveals slow protein turnover in hair-cell stereocilia. *Nature* **481,** 520–4 (2012).
18. Wittmaack, K. On the mechanism of cluster emission in sputtering. *Phys. Lett. A* **69,** 322–325 (1979).
19. Bandura, D. R. *et al.* Mass Cytometry: Technique for Real Time Single Cell Multitarget Immunoassay Based on Inductively Coupled Plasma Time-of-Flight Mass Spectrometry. *Anal. Chem.* **81,** 6813–6822 (2009).
20. Bendall, S. C. *et al.* Single-cell mass cytometry of differential immune and drug responses across a human hematopoietic continuum. *Science* **332,** 687–96 (2011).
21. Lou, X. *et al.* Polymer-Based Elemental Tags for Sensitive Bioassays. *Angew. Chemie Int. Ed.* **46,** 6111–6114 (2007).
22. Khan, A. A. & Quigley, J. G. Control of intracellular heme levels: heme transporters and heme oxygenases. *Biochim. Biophys. Acta* **1813,** 668–82 (2011).
23. Emmert-Buck, M. R. *et al.* Laser capture microdissection. *Science* **274,** 998–1001 (1996).
24. Frei, A. P. *et al.* Highly multiplexed simultaneous detection of RNAs and proteins in single cells. *Nat. Methods* **13,** 269–75 (2016).
25. Schulz, D. *et al.* Simultaneous Multiplexed Imaging of mRNA and Proteins with Subcellular Resolution in Breast Cancer Tissue Samples by Mass Cytometry. *Cell Syst.* **6,** 25–36.e5 (2018).

Figure 1

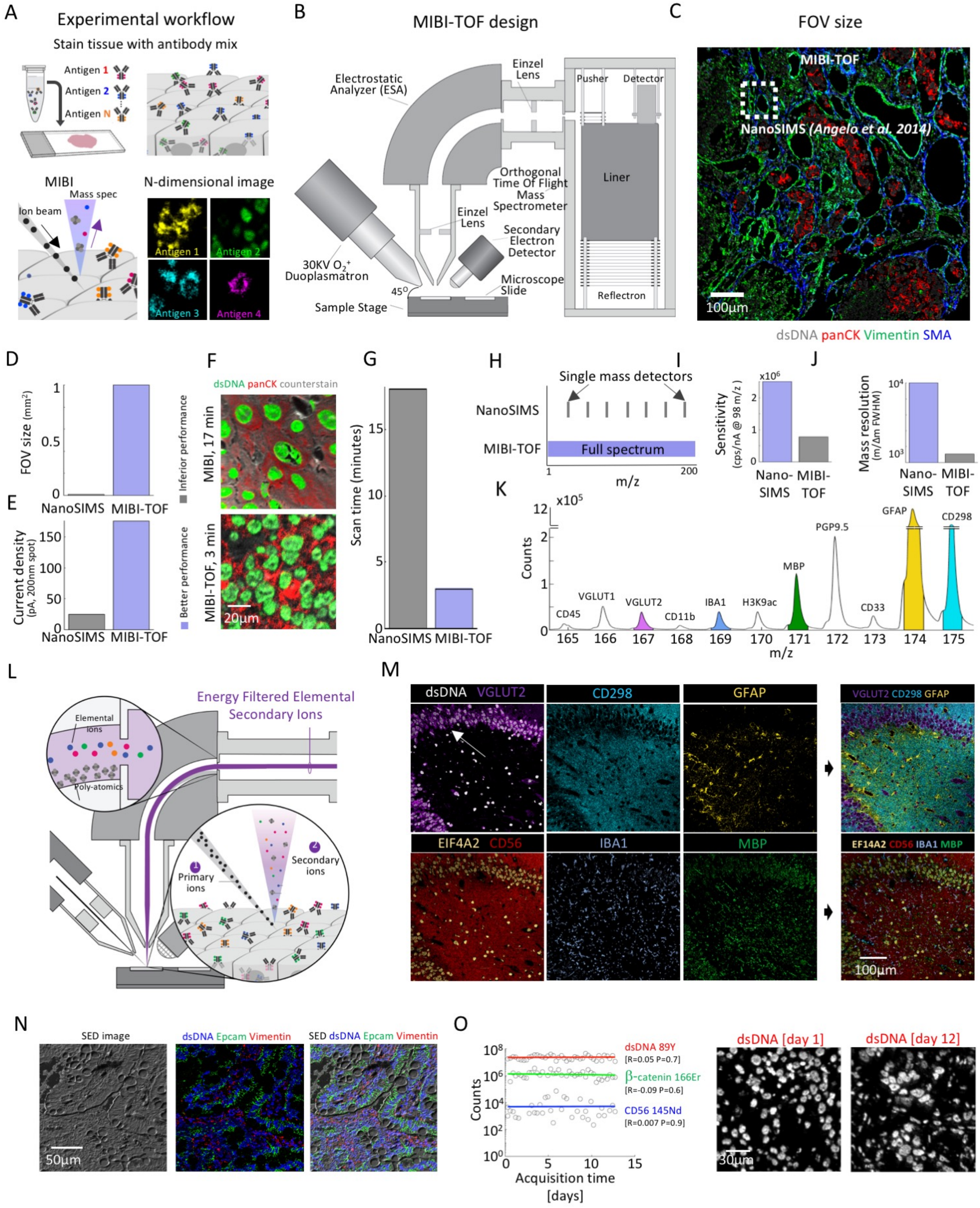
A
Experimental workflow
Stain tissue with antibody mix
Antigen 1
Antigen 2
Antigen N
MIBI
Mass spec
Ion beam
N-dimensional image
Antigen 1
Antigen 2
Antigen 3
Antigen 4
B
MIBI-TOF design
Electrostatic Analyzer (ESA)
Einzel Lens
Pusher
Detector
Liner
Orthogonal Time Of Flight Mass Spectrometer
Einzel Lens
Secondary Electron Detector
$30KV\ O_2^+$ Duoplasmatron
45°
Microscope Slide
Sample Stage
Reflectron
C
FOV size
MIBI-TOF
NanoSIMS (Angelo et al. 2014)
100µm
dsDNA panCK Vimentin SMA
D
FOV size (mm²)
1
0.5
0
NanoSIMS
MIBI-TOF
E
Current density (pA, 200nm spot)
150
100
50
0
NanoSIMS
MIBI-TOF
Inferior performance
Better performance
F
dsDNA panCK counterstain
MIBI, 17 min
MIBI-TOF, 3 min
20µm
G
Scan time (minutes)
15
10
5
0
NanoSIMS
MIBI-TOF
H
Single mass detectors
NanoSIMS
MIBI-TOF
Full spectrum
1
200
m/z
I
Sensitivity (cps/nA @ 98 m/z)
$x10^6$
2
1
0
Nano-SIMS
MIBI-TOF
J
Mass resolution (m/Δm FWHM)
10^4
10^3
Nano-SIMS
MIBI-TOF
K
Counts
$x10^5$
12
2
1
0
CD45
VGLUT1
VGLUT2
CD11b
IBA1
H3K9ac
MBP
PGP9.5
CD33
GFAP
CD298
165
166
167
168
169
170
171
172
173
174
175
m/z
L
Energy Filtered Elemental Secondary Ions
Elemental ions
Poly-atomics
Primary ions
Secondary ions
M
dsDNA VGLUT2
CD298
GFAP
VGLUT2 CD298 GFAP
EIF4A2 CD56
IBA1
MBP
EF14A2 CD56 IBA1 MBP
100µm
N
SED image
dsDNA Epcam Vimentin
SED dsDNA Epcam Vimentin
50µm
O
10^8
10^6
10^4
10^2
10^0
Counts
dsDNA 89Y
[R=0.05 P=0.7]
β-catenin 166Er
[R=-0.09 P=0.6]
CD56 145Nd
[R=0.007 P=0.9]
0
5
10
15
Acquisition time [days]
dsDNA [day 1]
dsDNA [day 12]
30µm

Figure 2

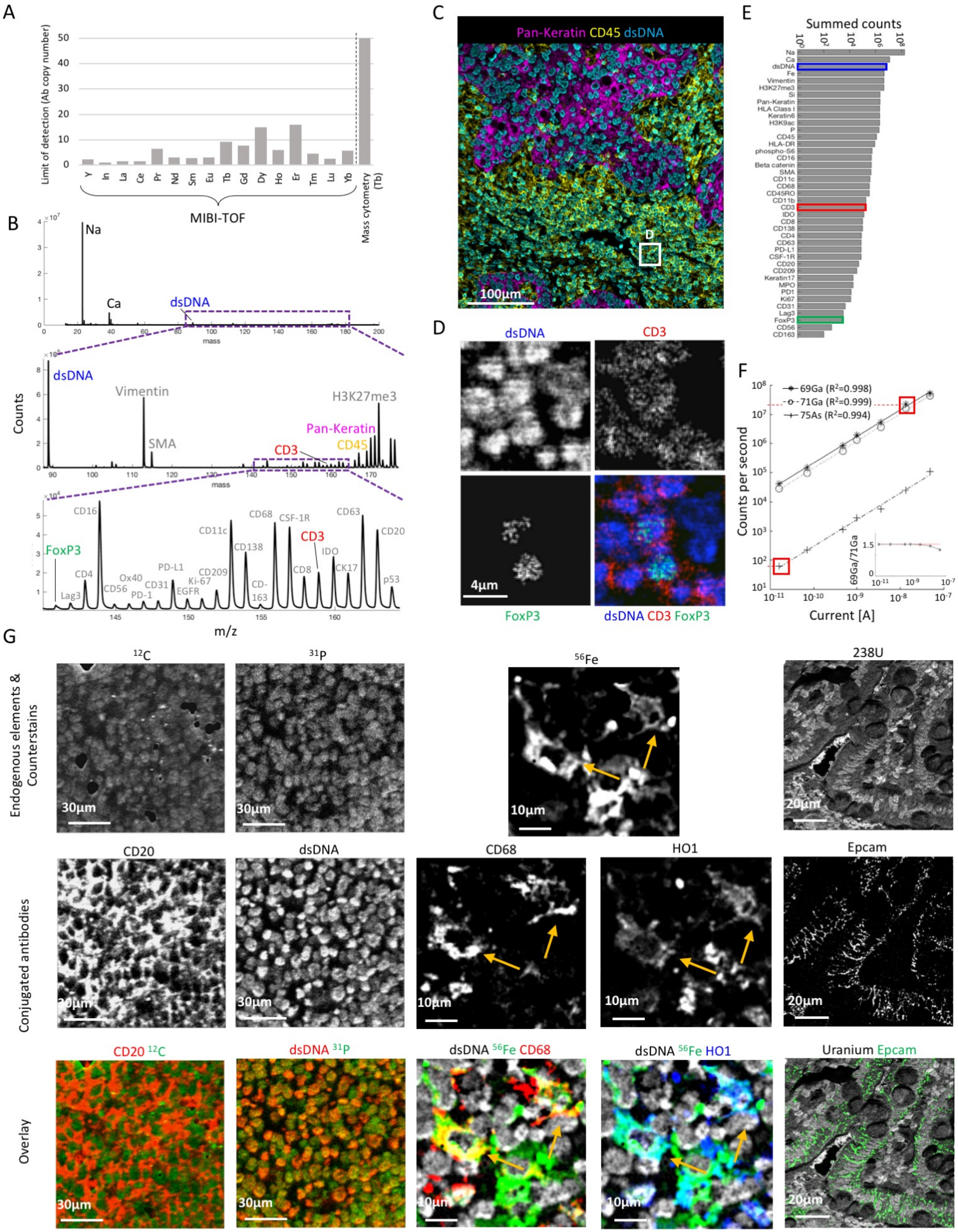
A
Limit of detection (Ab copy number)
50
40
30
20
10
0
Y
In
La
Ce
Pr
Nd
Sm
Eu
Tb
Gd
Dy
Ho
Er
Tm
Lu
Yb
MIBI-TOF
Mass cytometry (Tb)
B
×10^7
4
3
2
1
0
Na
Ca
dsDNA
0
20
40
60
80
100
120
140
160
180
200
mass
×10^5
8
6
4
2
0
dsDNA
Vimentin
SMA
H3K27me3
Pan-Keratin
CD45
CD3
90
100
110
120
130
140
150
160
170
mass
Counts
×10^4
5
4
3
2
1
FoxP3
Lag3
CD4
CD16
CD56
Ox40
PD-1
CD31
PD-L1
EGFR
Ki-67
CD209
CD11c
CD138
CD-163
CD68
CSF-1R
CD3
CD8
IDO
CK17
CD63
CD20
p53
145
150
155
160
m/z
C
Pan-Keratin CD45 dsDNA
D
100µm
D
dsDNA
CD3
FoxP3
dsDNA CD3 FoxP3
4µm
E
Summed counts
10^0
10^2
10^4
10^6
10^8
Na
Ca
dsDNA
Fe
Vimentin
H3K27me3
Si
Pan-Keratin
HLA Class I
Keratin6
H3K9ac
P
CD45
HLA-DR
phospho-S6
CD16
Beta catenin
SMA
CD11c
CD68
CD45RO
CD11b
CD3
IDO
CD8
CD138
CD4
CD63
PD-L1
CSF-1R
CD20
CD209
Keratin17
MPO
PD1
Ki67
CD31
Lag3
FoxP3
CD56
CD163
F
69Ga (R²=0.998)
71Ga (R²=0.999)
75As (R²=0.994)
Counts per second
10^8
10^7
10^6
10^5
10^4
10^3
10^2
10^1
Current [A]
10^-11
10^-10
10^-9
10^-8
10^-7
69Ga/71Ga
1.5
0
10^-11
10^-9
10^-7
G
Endogenous elements & Counterstains
12C
31P
56Fe
238U
30µm
30µm
10µm
20µm
Conjugated antibodies
CD20
dsDNA
CD68
HO1
Epcam
20µm
30µm
10µm
10µm
20µm
Overlay
CD20 12C
dsDNA 31P
dsDNA 56Fe CD68
dsDNA 56Fe HO1
Uranium Epcam
30µm
30µm
10µm
10µm
20µm

Figure 3

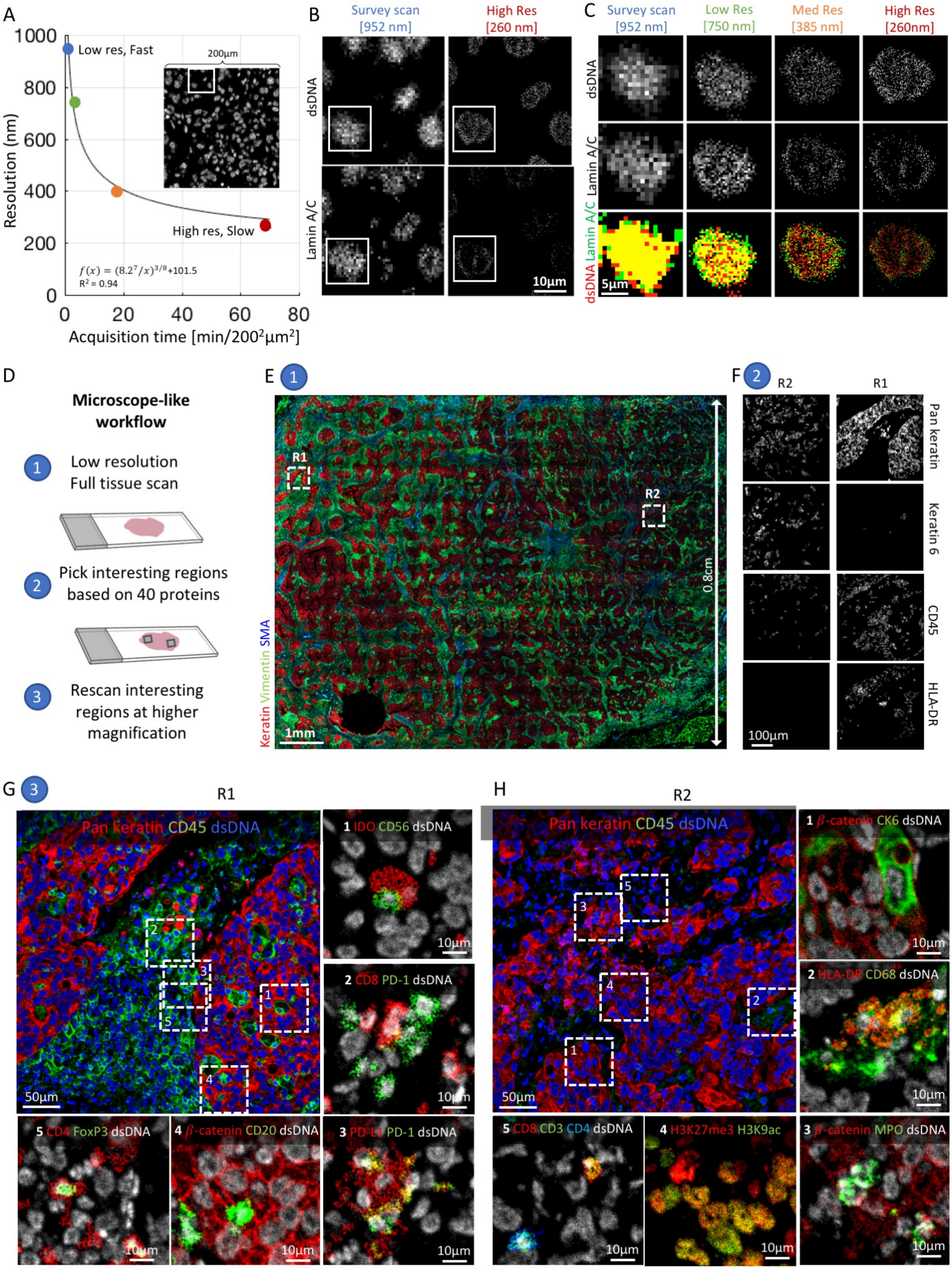
A
1000
800
600
400
200
0
Resolution (nm)
0
20
40
60
80
Acquisition time [min/200²µm²]
Low res, Fast
High res, Slow
200µm
$f(x) = (8.2^7/x)^{3/8}$+101.5
R² = 0.94
B
Survey scan [952 nm]
High Res [260 nm]
dsDNA
Lamin A/C
10µm
C
Survey scan [952 nm]
Low Res [750 nm]
Med Res [385 nm]
High Res [260nm]
dsDNA
Lamin A/C
dsDNA Lamin A/C
5µm
D
Microscope-like workflow
1 Low resolution Full tissue scan
2 Pick interesting regions based on 40 proteins
3 Rescan interesting regions at higher magnification
E 1
R1
R2
0.8cm
Keratin Vimentin SMA
1mm
F 2
R2
R1
Pan keratin
Keratin 6
CD45
HLA-DR
100µm
G 3
R1
Pan keratin CD45 dsDNA
1
2
3
4
5
50µm
1 IDO CD56 dsDNA
2 CD8 PD-1 dsDNA
5 CD4 FoxP3 dsDNA
4 β-catenin CD20 dsDNA
3 PD-L1 PD-1 dsDNA
10µm
H
R2
Pan keratin CD45 dsDNA
1
2
3
4
5
50µm
1 β-catenin CK6 dsDNA
2 HLA-DR CD68 dsDNA
5 CD8 CD3 CD4 dsDNA
4 H3K27me3 H3K9ac
3 β-catenin MPO dsDNA
10µm

Figure 4

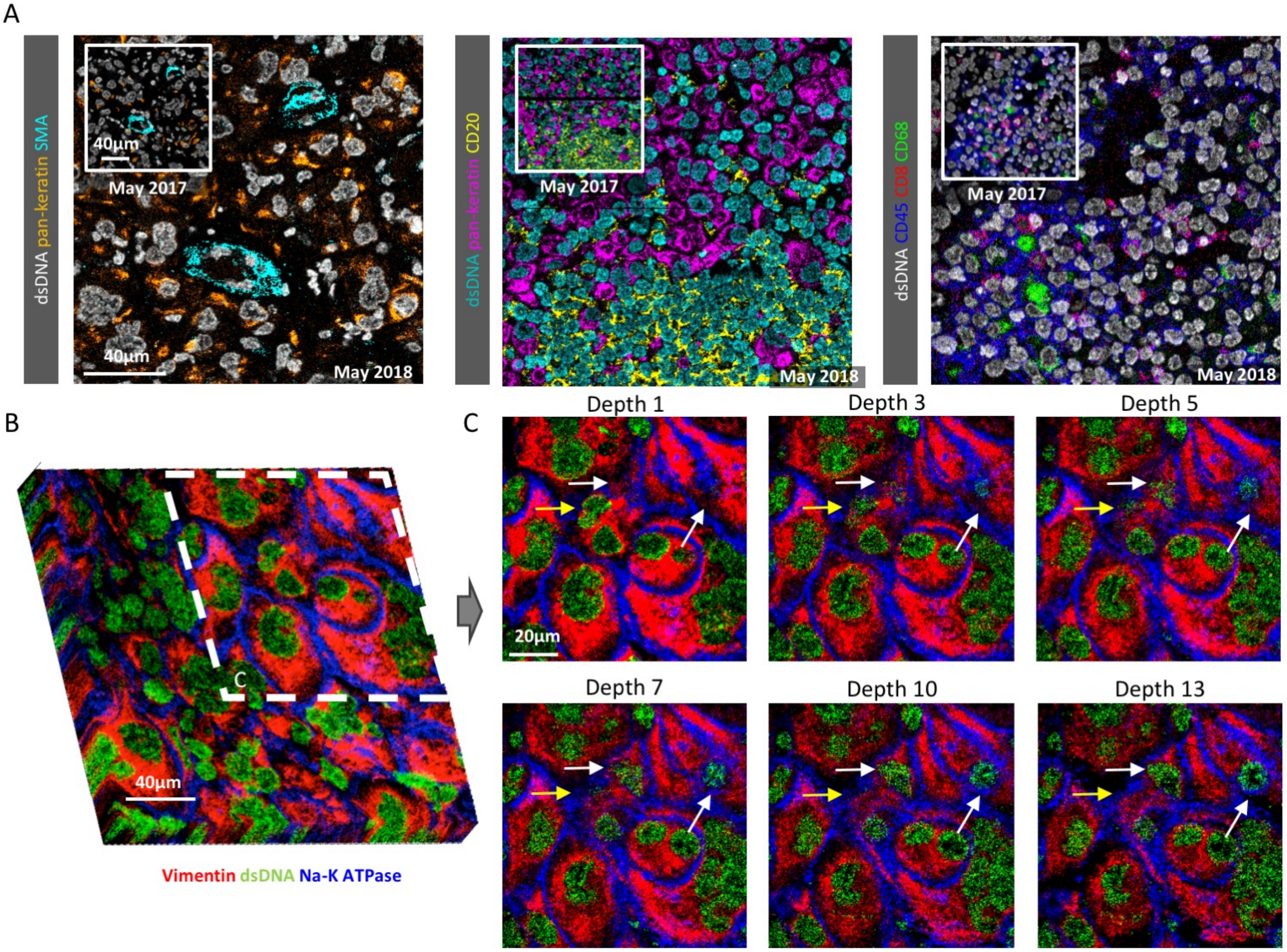
A
dsDNA pan-keratin SMA
40µm
May 2017
40µm
May 2018
dsDNA pan-keratin CD20
May 2017
May 2018
dsDNA CD45 CD8 CD68
May 2017
May 2018
B
C
40µm
Vimentin dsDNA Na-K ATPase
C
Depth 1
Depth 3
Depth 5
20µm
Depth 7
Depth 10
Depth 13

Figure S1

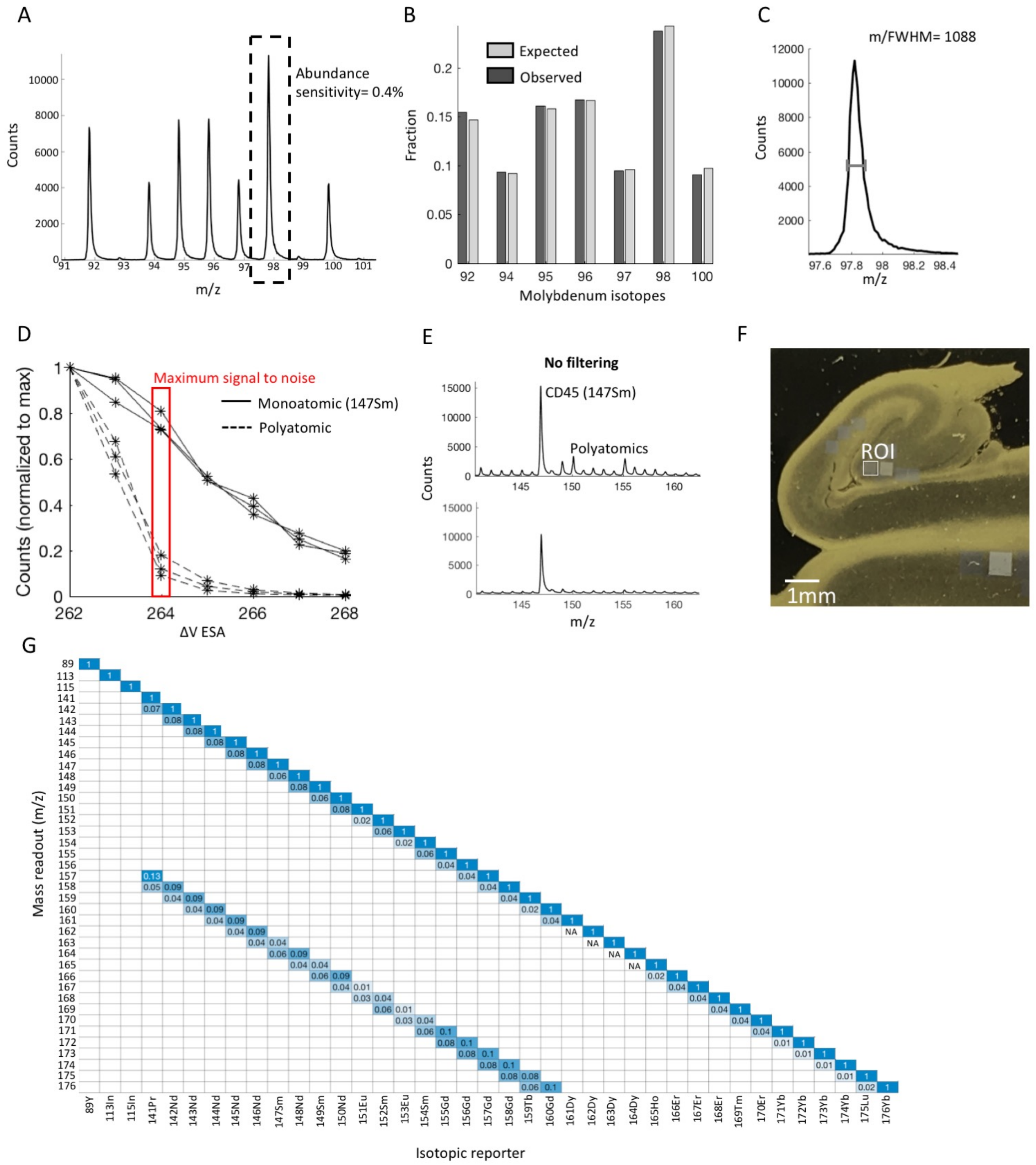

Mass readout (m/z)	89Y	113In	115In	141Pr	142Nd	143Nd	144Nd	145Nd	146Nd	147Sm	148Nd	149Sm	150Nd	151Eu	152Sm	153Eu	154Sm	155Gd	156Gd	157Gd	158Gd	159Tb	160Gd	161Dy	162Dy	163Dy	164Dy	165Ho	166Er	167Er	168Er	169Tm	170Er	171Yb	172Yb	173Yb	174Yb	175Lu	176Yb
89	1																																						
113		1																																					
115			1																																				
141				1																																			
142				0.07	1																																		
143					0.08	1																																	
144						0.08	1																																
145							0.08	1																															
146								0.08	1																														
147									0.08	1																													
148										0.06	1																												
149											0.08	1																											
150												0.06	1																										
151													0.08	1																									
152														0.02	1																								
153															0.06	1																							
154																0.02	1																						
155																	0.06	1																					
156																		0.04	1																				
157				0.13																0.04	1																			
158				0.05	0.09																0.04	1																		
159					0.04	0.09																0.04	1																	
160						0.04	0.09																0.02	1																
161							0.04	0.09																0.04	1															
162								0.04	0.09																NA	1														
163									0.04	0.04																NA	1													
164										0.06	0.09																NA	1												
165											0.04	0.04																NA	1											
166												0.06	0.09																0.02	1										
167													0.04	0.01																0.04	1									
168														0.03	0.04																0.04	1								
169															0.06	0.01																0.04	1							
170																0.03	0.04																0.04	1						
171																	0.06	0.1																0.04	1					
172																		0.08	0.1																0.01	1				
173																			0.08	0.1																0.01	1			
174																				0.08	0.1																0.01	1		
175																					0.08	0.08																0.01	1	
176																						0.06	0.1																0.02	1

Isotopic reporter

Figure S2

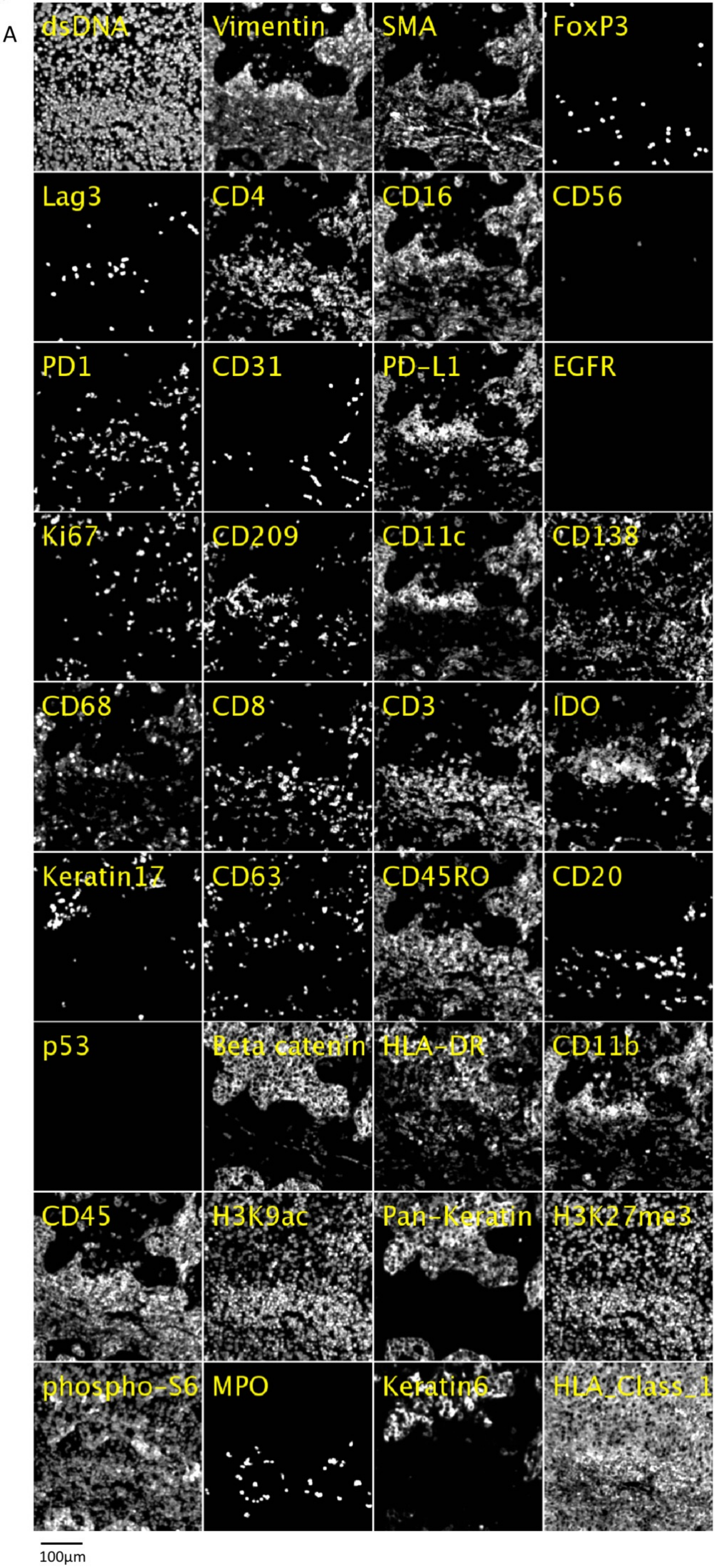
A
dsDNA
Vimentin
SMA
FoxP3
Lag3
CD4
CD16
CD56
PD1
CD31
PD-L1
EGFR
Ki67
CD209
CD11c
CD138
CD68
CD8
CD3
IDO
Keratin17
CD63
CD45RO
CD20
p53
Beta catenin
HLA-DR
CD11b
CD45
H3K9ac
Pan-Keratin
H3K27me3
phospho-S6
MPO
Keratin6
HLA_Class_1
100µm

Figure S3

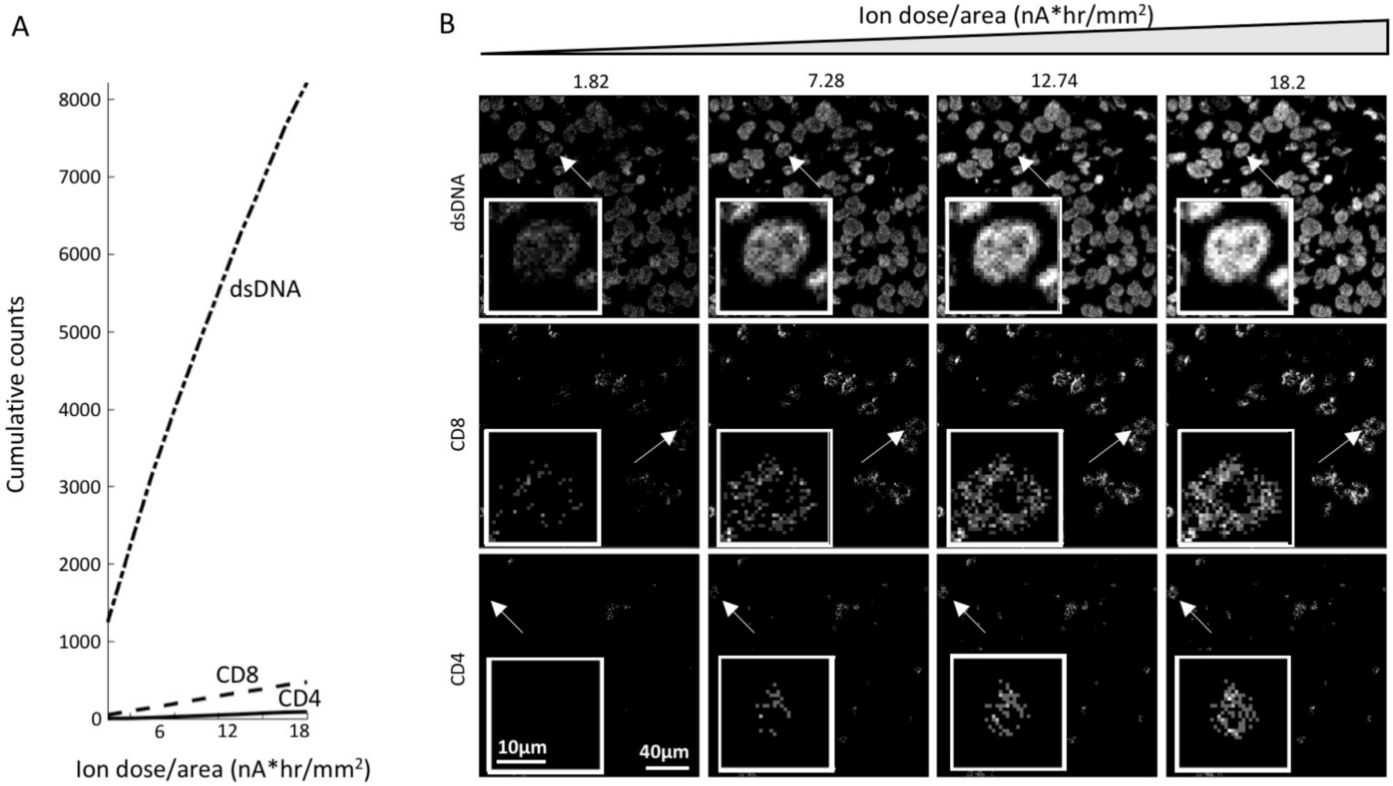
A
Cumulative counts
8000
7000
6000
5000
4000
3000
2000
1000
0
6
12
18
dsDNA
CD8
CD4
Ion dose/area (nA*hr/mm2)
B
Ion dose/area (nA*hr/mm2)
1.82
7.28
12.74
18.2
dsDNA
CD8
CD4
10μm
40μm